nature communications

Article

https://doi.org/10.1038/s41467-024-52947-6

Structural basis of μ-opioid receptor targeting by a nanobody antagonist

Received: 16 December 2023

Accepted: 24 September 2024

Published online: 09 October 2024

Check for updates

Jun Yu[1,10], Amit Kumar[2,10], Xuefeng Zhang[1], Charlotte Martin[3], Kevin Van holsbeeck[3], Pierre Raia[4], Antoine Koehl[5], Toon Laeremans[6], Jan Steyaert[7,8], Aashish Manglik[9], Steven Ballet[3], Andreas Boland[1,11] ✉ & Miriam Stoeber[2,11] ✉

The μ-opioid receptor (μOR), a prototypical G protein-coupled receptor (GPCR), is the target of opioid analgesics such as morphine and fentanyl. Due to the severe side effects of current opioid drugs, there is considerable interest in developing novel modulators of μOR function. Most GPCR ligands today are small molecules, however biologics, including antibodies and nanobodies, represent alternative therapeutics with clear advantages such as affinity and target selectivity. Here, we describe the nanobody NbE, which selectively binds to the μOR and acts as an antagonist. We functionally characterize NbE as an extracellular and genetically encoded μOR ligand and uncover the molecular basis for μOR antagonism by determining the cryo-EM structure of the NbE-μOR complex. NbE displays a unique ligand binding mode and achieves μOR selectivity by interactions with the orthosteric pocket and extracellular receptor loops. Based on a β-hairpin loop formed by NbE that deeply protrudes into the μOR, we design linear and cyclic peptide analogs that recapitulate NbE's antagonism. The work illustrates the potential of nanobodies to uniquely engage with GPCRs and describes lower molecular weight μOR ligands that can serve as a basis for therapeutic developments.

G protein-coupled receptors (GPCRs) represent key therapeutic targets due to their central roles in cellular signaling and control over a plethora of physiological processes. Developing new ligands that bind a given GPCR with high selectivity remains a significant challenge in drug discovery[1–3]. Small molecule ligands have historically dominated the landscape of GPCR-targeted drugs, but recently biologics, including antibodies and nanobodies (Nbs), have emerged as an alternative class of ligands that offer distinct advantages and hold promise for therapeutic developments[4,5]. Nbs are single-domain antibody fragments derived from heavy chain-only antibodies, which naturally occur in camelids and cartilaginous fish, and are characterized by small size, high antigen binding affinity, and binding loops that can access deep cavities on target proteins[6]. Nbs can show enhanced selectivity over small molecules due to their ability to interact with unique and extended epitope surfaces. Over the last decade, Nbs that bind GPCRs on their intracellular side have served as innovative research tools to uncover GPCR signal transduction mechanisms[7,8]. For example, Nbs were used as crystallization chaperones or as fiducial markers in high-

[1]Department of Molecular and Cellular Biology, University of Geneva, Geneva, Switzerland. [2]Department of Cell Physiology and Metabolism, University of Geneva, Geneva, Switzerland. [3]Departments of Chemistry and Bioengineering Sciences, Vrije Universiteit Brussel, Brussels, Belgium. [4]Department of Plant Sciences, University of Geneva, Geneva, Switzerland. [5]Department of Electrical Engineering and Computer Sciences, University of California, Berkeley, CA, USA. [6]Confo Therapeutics N.V., Gent, Belgium. [7]Structural Biology Brussels, Vrije Universiteit Brussel, Brussels, Belgium. [8]VIB-VUB Center for Structural Biology, VIB, Brussels, Belgium. [9]Department of Pharmaceutical Chemistry, University of California, San Francisco, CA, USA. [10]These authors contributed equally: Jun Yu, Amit Kumar. [11]These authors jointly supervised this work: Andreas Boland, Miriam Stoeber. ✉e-mail: andreas.boland@unige.ch; miriam.stoeber@unige.ch

resolution structural studies[9–12]. Conformation-selective Nbs were also repurposed into biosensors to report GPCR activity in living cells[13,14]. Only recently, several Nbs that bind GPCRs as extracellular ligands and thereby modulate receptor function have been described[15–20]. Generating knowledge on GPCR-targeting Nbs is key to unlocking their potential as both versatile research tools and therapeutic compounds.

Opioid receptors (ORs) are prototypical members of the rhodopsin-like GPCR family and function in pain modulation and analgesia[21,22]. The OR family comprises four major receptor subtypes, including the μOR, δOR, κOR, and nociceptin-OR (NOPR), with the μOR representing the prime therapeutic target for pain relief. Approved drugs that target μORs are diverse small molecule compounds, including the widely used analgesics morphine and fentanyl. The ligand repertoire has recently been expanded through structure-based molecular docking, rational design, and high-throughput screening, delivering new OR ligands with distinct pharmacological profiles, including biased agonism, receptor subtype selectivity, and pharmacokinetic properties[23–25]. Discovering additional and innovative modulators of μOR function, including agonists and antagonists, remains a pressing necessity for developing improved analgesics and compounds that can reduce or reverse the deleterious opioid side effects[26]. Until now, no antibody or Nb ligand for ORs has been characterized in-depth, representing a hurdle in exploiting the unique features of biologics to effectively target ORs.

In this study, we functionally and structurally analyzed NbE, an extracellular μOR-targeting Nb ligand[9]. Using cellular binding and signaling assays, we identified that NbE selectively binds to μOR with nanomolar affinity and acts as an antagonist when added as ligand or expressed as a genetically-encoded cell surface displayed protein. Using cryogenic electron microscopy (cryo-EM), we then solved the structure of the NbE-μOR complex, which reveals that NbE deeply inserts into the orthosteric pocket and additionally interacts with two extracellular loops (ECL) of the μOR. We find that the ECL interactions significantly contribute to NbE binding and OR subtype selectivity. Based on NbE's complementary-determining region 3 (CDR3), which inserts as a β-hairpin loop into the orthosteric pocket, we synthesized a set of linear and cyclic peptide mimetics of different lengths. The CDR3-based cyclic peptides were grafted on a semi-rigid β-turn-inducing scaffold. Thereby, we identify peptides that bind the μOR with an affinity similar to NbE and retain μOR-selective antagonism. The work uncovers a distinct ligand engagement profile at the μOR and provides a strategy for developing biologics-based μOR ligands.

Results

NbE binds the extracellular side of μOR and is an antagonist

We first tested whether NbE, which was part of a Nb library previously generated against the μOR[9], binds to the extracellular side of μOR on the surface of living cells. We covalently conjugated purified NbE with Alexa Fluor 488 and incubated OR-expressing HEK293 cells with the fluorescently labeled NbE. Confocal microscopy analyses showed a pronounced NbE signal at the plasma membrane of cells expressing mouse or human μOR, while cells expressing the closely related δOR, κOR, or NOPR were not labeled by NbE (Fig. 1a and Supplementary Fig. 1a). Selective binding of NbE to μOR-expressing cells was also detected by flow cytometry analyzes after adding NbE at increasing concentrations (Fig. 1b). δOR-, κOR-, or NOPR-expressing cells gated for similar receptor surface levels did not exhibit NbE binding above control cells (Fig. 1b and Supplementary Fig. 1b). Since the NbE staining intensity of μOR expressing cells did not plateau at the highest NbE concentration tested (10 μM), we turned to grating-coupled interferometry (GCI) to determine the NbE binding strength. We immobilized biotinylated AVI-tagged NbE on a streptavidin-coated biosensor surface and perfused it with buffer containing purified murine μOR at different concentrations. From the binding curves, we extracted the affinity of the NbE-μOR interaction (K_D = 56 nM) and the kinetic parameters ($k_a = 2.8 \times 10^3\ M^{-1}s^{-1}$ and $k_d = 1.6 \times 10^{-4}\ s^{-1}$), which revealed a slow NbE off-rate (Supplementary Fig. 1c, d).

Next, we investigated if NbE binds competitively with orthosteric μOR ligands. We incubated μOR-expressing HEK293 cells with increasing concentrations of naloxone, subsequently added fluorescent NbE, and quantified the NbE signal by flow cytometry. NbE binding decreased in a naloxone concentration-dependent manner and was entirely abolished at high naloxone concentrations (Fig. 1c). The data suggested that the NbE binding site on the μOR potentially overlaps with the orthosteric ligand binding pocket, and thus we tested if NbE modulates μOR activity. We first assessed whether NbE behaves as an agonist by measuring μOR-mediated inhibition of cyclic AMP (cAMP) accumulation in living cells, a readout of Gi-driven OR signaling. Application of NbE did not activate μOR even at high concentrations, in contrast to the peptide agonist DAMGO (Fig. 1d). We then tested whether NbE acts as a μOR antagonist and reduces the signaling effects of opioid peptides and small molecule opioid drugs. Indeed, pre-incubation of μOR-expressing cells with NbE caused a concentration-dependent decrease in DAMGO- and morphine-induced Gi signaling (Fig. 1e). At high concentrations, NbE fully blocked DAMGO and morphine-driven μOR inhibition of cAMP production. Furthermore, NbE addition strongly reduced the recruitment of a G protein probe (miniGi) and β-arrestin2 to DAMGO-activated μOR, as measured by split nanoluciferase (NanoLuc)-based complementation assays (Supplementary Fig. 2a).

We hypothesized that NbE may also antagonize μOR function when ectopically expressed in cells and targeted to the extracellular leaflet of the plasma membrane via a glycolipid anchor. To test this, we fused NbE to a C-terminal glycosylphosphatidylinositol (GPI) signal peptide, separated by a flexible linker (Fig. 1f). We also added a secretory signal peptide at the N-terminus, followed by an HA-tag or a fluorescent protein to enable determining the subcellular localization of the NbE fusion proteins (Fig. 1f). Confocal microscopy analyses of NbE-GPI-expressing cells showed that NbE predominantly localized at the cell surface (Fig. 1g). Immunostaining of cells expressing HA-NbE-GPI with HA antibodies in non-permeabilizing conditions revealed that NbE was efficiently displayed on the extracellular side of the plasma membrane (Supplementary Fig. 2b). We also constructed a bivalent tandem NbE-NbE-GPI construct as well as a non-targeting Nb-GPI control (Nb-ctr), and both were predominantly cell surface localized (Supplementary Fig. 2c). μOR-expressing HEK293 cells transfected with monovalent or bivalent NbE-GPI constructs showed significantly higher cAMP levels after DAMGO treatment relative to cells expressing the Nb-GPI control, indicating a NbE-mediated block of μOR signaling (Fig. 1h).

Taken together, NbE specifically binds to the extracellular side of the μOR and competes with orthosteric opioid ligands. Furthermore, NbE acts as an antagonist when added to cells as an extracellular ligand or when ectopically expressed and targeted to the outer plasma membrane leaflet as GPI-anchored fusion protein.

Cryo-EM structure determination of the NbE-μOR complex

Advancement of structural biology techniques have led to the determination of several μOR structures in complex with either antagonists[11,27], partial agonists[25,28], or full agonists, including the endogenous peptides β-endorphin and endomorphin[9,28–30]. All ligands bind to the orthosteric ligand binding pocket that is on the extracellular side and largely solvent exposed. To identify the precise molecular binding mode of NbE, we determined the structure of the NbE-μOR complex using cryo-EM. Initial structure determination was precluded due to the absence of large extracellular features of the complex. The surrounding detergent micelle additionally impaired accurate particle projection alignments, resulting in unsuccessful 3D reconstruction. To provide extra features for accurate particle alignment, we incubated the purified NbE-μOR complex with a Fab module

https://doi.org/10.1038/s41467-024-52947-6

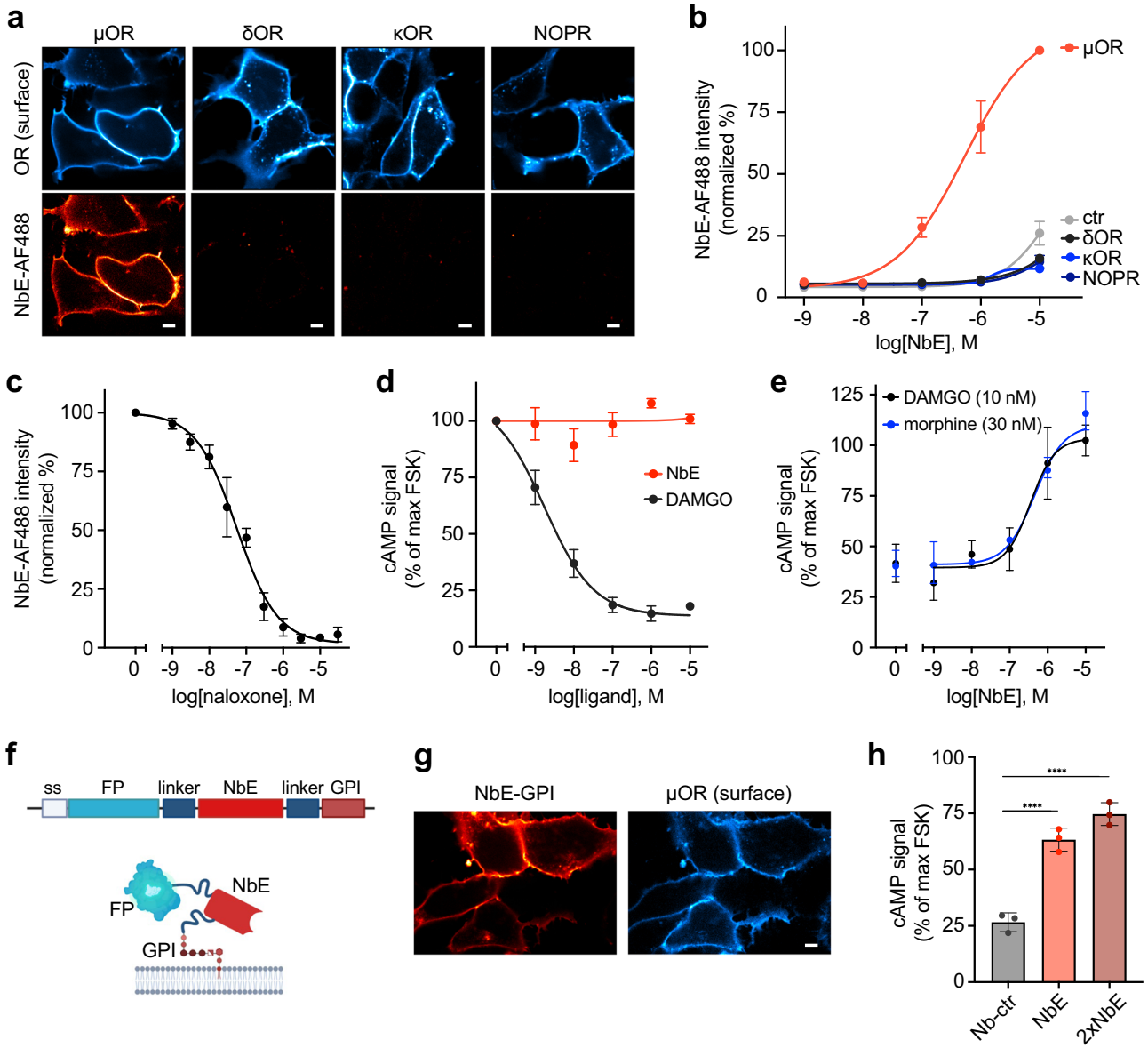

Fig. 1 | NbE binds the extracellular side of the μOR and acts as an antagonist. **a** Confocal images of HEK293 cells expressing FLAG-μOR, δOR, κOR, or NOPR (labeled with anti-FLAG M1-AF647, cyan) and incubated with 1 μM purified AF488-labeled NbE (red). Scale bar, 10 μm. **b** FACS-based quantification of AF488-NbE binding to HEK293 cells expressing murine μOR, δOR, κOR, or NOPR at different NbE concentrations (cells gated for similar receptor surface levels), $N = 3$, mean ± SEM. **c** FACS-based quantification of AF488-NbE binding (1 μM) to HEK293-μOR cells pretreated with naloxone at different concentrations. $N = 4$, mean ± SEM. **d** Maximum cAMP response in HEK293 stably expressing μOR, stimulated with 2.5 μM forskolin (FSK, norm. to 100%), treated with increasing concentrations of DAMGO ($N = 5$) or NbE ($N = 3$), mean ± SEM. **e** Maximum cAMP response in HEK293 stably expressing μOR, stimulated with 2.5 μM FSK (norm. to 100%), treated with 10 nM DAMGO ($N = 4$) or 30 nM morphine ($N = 2$) (corresponds to agonists' EC50, respectively) and pre-incubated with increasing concentrations of NbE, mean ± SEM. **f** Targeting NbE to the extracellular leaflet of the plasma membrane by fusion to a GPI anchor motif. ss = signal sequence, FP = fluorescent protein. Created in BioRender. Stoeber, M. (2024) BioRender.com/o10b826. **g** Confocal images of HEK293 cells stably expressing μOR (labeled with anti-FLAG M1-AF647, cyan) and transfected with mRuby2-NbE-GPI (red). Scale bar, 10 μm. **h** Maximum cAMP response in μOR-expressing HEK293, expressing GPI-anchored Nb-ctr, NbE, or bivalent NbE (2xNbE). All conditions treated with 10 nM DAMGO and normalized to cAMP level upon addition of 2.5 μM FSK. $N = 3$, mean ± SEM, $p < 0.0001$, by ordinary one-way ANOVA. In all panels, N indicates the number of independent experiments. Source data are provided as a Source Data file.

consisting of a Nb-binding Fab fragment (NabFab) and an anti-Fab Nb, recently developed as a fiducial marker[31]. The resulting stable and homogenous NbE-μOR-Fab module complex was purified by size exclusion chromatography (Supplementary Fig. 3a). Cryo-EM analyzes enabled us to determine the structure of the NbE-μOR-Fab module complex at a global resolution of 3.1 Å (Supplementary Fig. 3b–f, Supplementary Fig. 4a–c, Supplementary Table 1). The EM-derived Coulomb potential map provides excellent side chain densities for most parts of the complex with the best resolved region at the NbE-μOR interface (Supplementary Fig. 3d, f and Supplementary Fig. 5a).

The overall structure of the NbE-μOR complex bound to the Fab module is shown in Fig. 2a. The NabFab attaches to the NbE scaffold at a site distal to the CDR loops. NabFab binding to NbE is ensured by introducing three point mutations in NbE's scaffold, thereby assimilating NbE to the scaffold of Tc-Nb4, the original target antigen of NabFab[31]. Introducing the scaffold mutations did not significantly alter NbE binding (Ki) to μOR in cell membranes, as measured in homogeneous time-resolved fluorescence (HTRF) Tag-lite ligand competition binding assays (Supplementary Fig. 4d). The pre-assembled NbE-NabFab complex showed a modest reduction in the Ki (Supplementary

https://doi.org/10.1038/s41467-024-52947-6

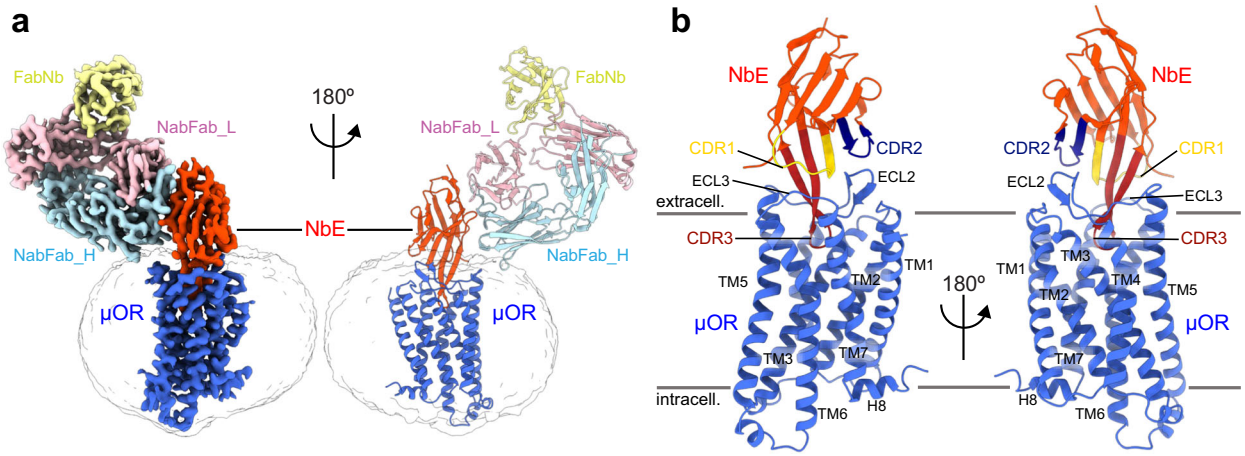

Fig. 2 | Architecture of the NbE-μOR complex. a Cryo-EM map (left) and ribbon representation (right) of the NbE-μOR-Fab module complex, with the murine μOR colored in blue, NbE in red, the heavy and light chains of the Fab fragment in sky blue and light pink, respectively, and the anti-Fab nanobody (FabNb) in yellow (**b**) The NbE-μOR complex as ribbon representation, with a focus on the NbE-μOR interface. NbE deeply inserts its CDR3 β-hairpin loop into the orthosteric binding pocket. For reasons of clarity the Fab module is omitted. CDR1, 2, and 3 are highlighted in yellow, dark blue and dark red, respectively. Otherwise color-coded as in (**a**).

Fig. 4d), possibly due to the larger ligand size and slight steric clashes between the membrane surrounding μOR and the NabFab fragment, as suggested by the EM density map (Fig. 2a and Supplementary Movie 1). The Fab module binds in a single and rigid conformation to NbE, enabling high-resolution structure determination of the NbE-μOR complex. For reasons of clarity, the Fab module is omitted in all subsequent figures (Fig. 2b and Supplementary Movie 1).

When bound to NbE, the μOR adopts an inactive conformation, which closely resembles the structures of the μOR bound to the morphinan antagonist β-funaltrexamine (β-FNA) or alvimopan (Supplementary Fig. 6a)[11,27]. The average root mean square deviation (RMSD) for all C_α atoms of μOR between the NbE-μOR complex and the μOR complexes bound to antagonists is 0.78 Å, whereas the RMSD between NbE-μOR and agonist-bound structures is on average 1.72 Å (Supplementary Table 2). In particular, transmembrane helix 6 (TM6), which is displaced by roughly 10 Å in the activated state[9,29], superimposes well between the NbE-μOR and the β-FNA- or alvimopan-bound inactive μOR structures (Supplementary Fig. 6a, c). Moreover, a conserved core triad consisting of the amino acids I155$^{3.40}$, P244$^{5.50}$, and F289$^{6.44}$ (Ballesteros-Weinstein numbering scheme[32]), which lies below the ligand binding pocket and propagates structural rearrangements involved in receptor activation[9], superimposes well with the μOR in the inactive form (Supplementary Fig. 6b, d). Structural differences in the ligand binding pocket between agonists, partial agonists, and antagonists are relatively subtle[33,34], however, binding of NbE to the μOR induces several unique conformational changes in the orthosteric binding pocket and the extracellular loops.

Unique interaction profile of NbE with the inactive μOR

Binding of NbE to the μOR is mediated through its complementarity-determining regions (CDRs) CDR1 and CDR3, with the main interaction interface being formed between the β-hairpin loop of CDR3 and μOR's TM helices 3, 5, 6, and 7 (Fig. 3a–d and Supplementary Table 3). CDR3 deeply inserts into the orthosteric ligand binding pocket with the three aromatic residues Y106^{NbE}, F107^{NbE} and Y108^{NbE} forming the tip of the loop (Fig. 3b, e and Supplementary Movie 1).

Similar to previously determined μOR structures bound to the ligands DAMGO[29], BU72[9], β-FNA[27], alvimopan[11], PZM21, and FH210[25], as well as β-endorphin and endomorphin[30], H297$^{6.52}$ is positioned closely to a phenol hydroxyl group of the NbE ligand (Fig. 3b and Supplementary Fig. 5b). While binding of BU72 and β-FNA is mediated through a hydrogen bond network that involves two water molecules[9,27], in the NbE-μOR complex, H297$^{6.52}$and Y106^{NbE} are directly forming a hydrogen bond (Fig. 3b and Supplementary Fig. 5b). In addition, Y106^{NbE} is surrounded by mainly hydrophobic residues, including Y148$^{3.33}$, M151$^{3.36}$, V236$^{5.42}$, F237$^{5.43}$, I296$^{6.51}$, and V300$^{6.55}$ (Fig. 3b). F107^{NbE}, the second tip-forming aromatic residue, inserts itself into a neighboring hydrophobic cavity (Fig. 3b, e) and interacts with the key residues I143$^{3.30}$, Y148$^{3.33}$, M151$^{3.36}$, W293$^{6.48}$, I322$^{7.39}$ and Y326$^{7.43}$ of μOR (Fig. 3b). Interestingly, the aspartate D147$^{3.32}$, present in many class A GPCRs, and crucial for the recognition of DAMGO, β-FNA, BU72, PZM21, and endogenous peptides by forming a salt bridge with an amine group of the ligand, is rotated compared to all other μOR structures (Supplementary Fig. 6e). Instead of forming a salt bridge with the ligand, D147$^{3.32}$ stacks in this conformation onto F107^{NbE}, representing a distinct ligand-receptor interaction mode (Fig. 3b and Supplementary Fig. 6e). The third aromatic residue Y108^{NbE} is situated at the periphery of the orthosteric binding pocket (Fig. 3c). The aromatic ring of the phenol group stacks against L219^{ECL2}, part of ECL2, whereas the hydroxyl group forms a hydrogen bond with K233$^{5.39}$ (Fig. 3b, c and Supplementary Fig. 5b). K233$^{5.39}$ had previously been identified as the side chain to which the morphinan ligand β-FNA is covalently attached[27,35]. Another notable difference in the ligand binding pocket involves W318$^{7.35}$ which is uniquely positioned, likely due to steric constraints when inserting the large NbE ligand into the narrow ligand binding pocket (Supplementary Fig. 6e). This specific rotamer conformation has only been observed when the pentameric peptide ligand DAMGO is bound to the μOR, however, in the NbE-μOR structure W318$^{7.35}$ is shifted by several Å. Because of the unusual positioning of W318$^{7.35}$ and its rotamer conformation, K303$^{6.58}$ that often stacks onto W318$^{7.35}$ is displaced by several Å, hydrogen bonding with S103^{NbE} of NbE instead (Fig. 3d and Supplementary Fig. 5b).

The three tip-forming aromatic residues of NbE are recognized by neighboring but distinct binding cavities in the orthosteric binding pocket (Fig. 3e). Here, Y106^{NbE} and F107^{NbE} are binding to sites usually occupied by small molecule ligands (Fig. 3f–h), whereas Y108^{NbE} stacks onto L219 of ECL2, thereby stabilizing the CDR3 β-hairpin loop in its conformation. The binding of ligands to this peripheral binding site has not yet been observed in other μOR structures. Conversely, the ligands alvimopan (antagonist), endomorphin, and fentanyl (agonists) are inserting aromatic functional groups into another binding cavity, which is not occupied by NbE (Fig. 3f–h).

https://doi.org/10.1038/s41467-024-52947-6

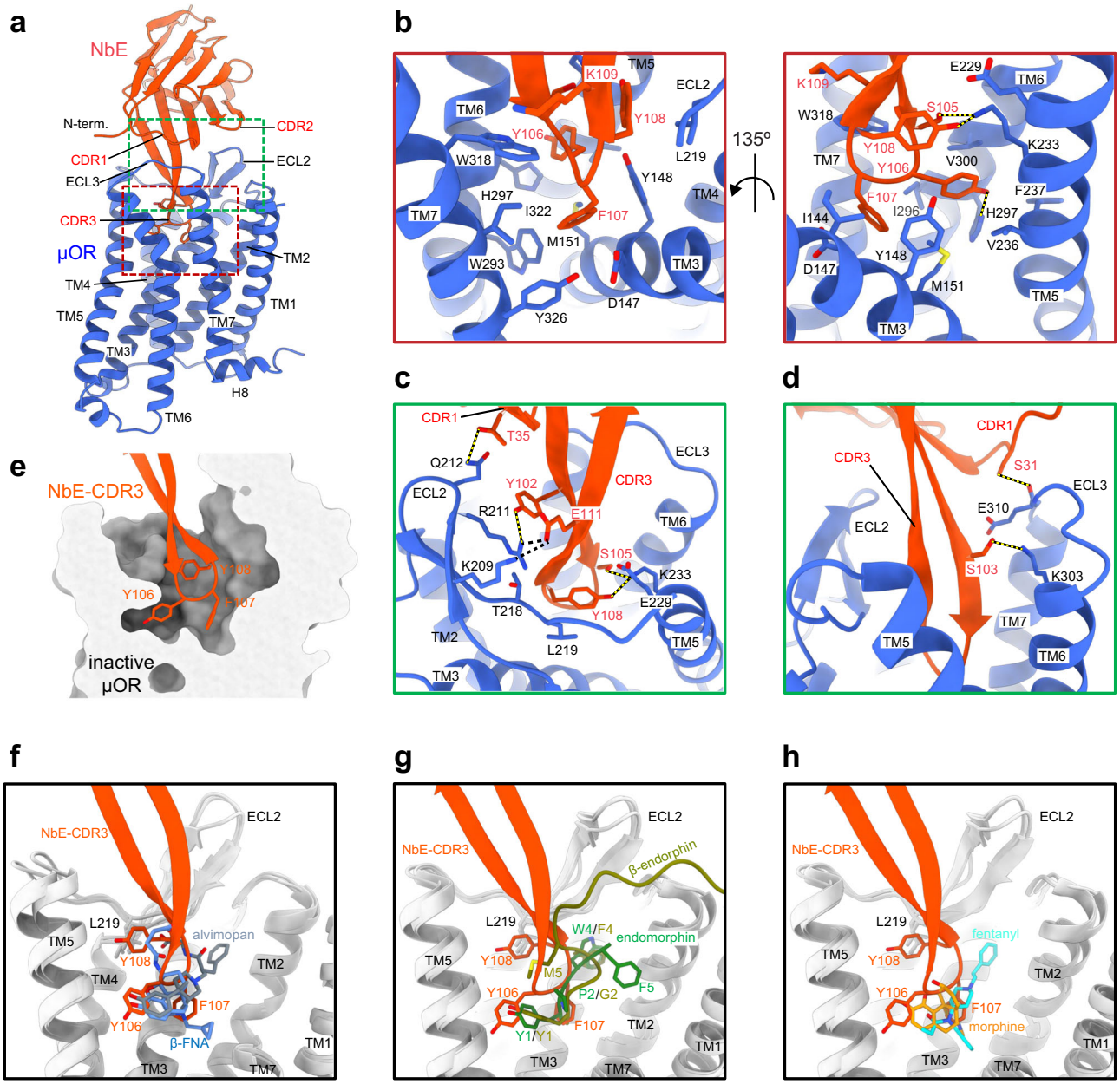

Fig. 3 | The NbE-μOR interaction interface. a Overview of the NbE-μOR complex, color-coded as in Fig. 2. Dashed red and green squares indicate the close-up views shown in panels (**b**–**d**). **b** Orthosteric binding pocket close-up; NbE's F107 (left panel) and Y106 (right panel) are centered. Interface residues shown as sticks. **c** Top view of the μOR ligand binding pocket with CDR3^{NbE} deeply inserted. Interactions between ECL2 of the μOR and CDR3 of NbE are highlighted. Interface residues are shown as sticks, hydrogen bonds and salt bridges are indicated as yellow dashed lines and black dashed lines, respectively. **d** Interaction interface between ECL3 of μOR and CDR3 of NbE. Interface residues are shown as sticks, hydrogen bonds and salt bridges are indicated as yellow dashed lines and black dashed lines, respectively. **e** Tip-forming NbE residues Y106, F107, and Y108 (shown as sticks) of CDR3 are binding to hydrophobic patches inside the orthosteric ligand binding pocket of μOR (shown as surface representation). **f** Binding mode superposition of NbE and the small molecule antagonists β-FNA (PDB: 4DKL) and alvimopan (PDB: 7UL4). Y108^{NbE} stacks against μOR's L219^{ECL2}, which is a unique ligand-receptor interaction. Alvimopan inserts a phenyl group in a binding cleft not occupied by NbE or β-FNA. **g** Binding mode superposition of NbE and peptide agonists β-endorphin (PDB: 8F7Q) or endomorphin (PDB: 8F7R). Y108^{NbE} uniquely recognizes L219^{ECL2}, whereas a phenol group of endomorphin binds to a similar site also recognized by alvimopan (**f**) or fentanyl (**h**). **h** Binding mode superposition of NbE and the small molecule agonists fentanyl (PDB: 8EF5) or morphine (PDB: 8EF6).

To probe if the Nb ligand undergoes conformational rearrangements upon μOR binding, we crystallized NbE in its unbound form. The crystal contained three NbE molecules per asymmetric unit with all molecules virtually identical to each other, including the CDRs. A superposition between the unbound and bound NbE structures revealed that the CDR1 region and the CDR3 β-hairpin loop undergo a conformational shift when comparing the free and the μOR-bound state, while the Nb scaffold is nearly identical (Supplementary Fig. 7). The conformational differences suggest that CDR1 and CDR3 exhibit intrinsic flexibility, which could potentially be important for conformational selection of the inactive μOR and high-affinity binding of NbE.

In summary, NbE shows a unique interaction profile with the μOR. In particular, D147$^{3.32}$, L219^{ECL2}, and W318$^{7.35}$ of the μOR engage with NbE in a so far undetected ligand binding mode that can offer new possibilities for structure-guided drug design.

https://doi.org/10.1038/s41467-024-52947-6

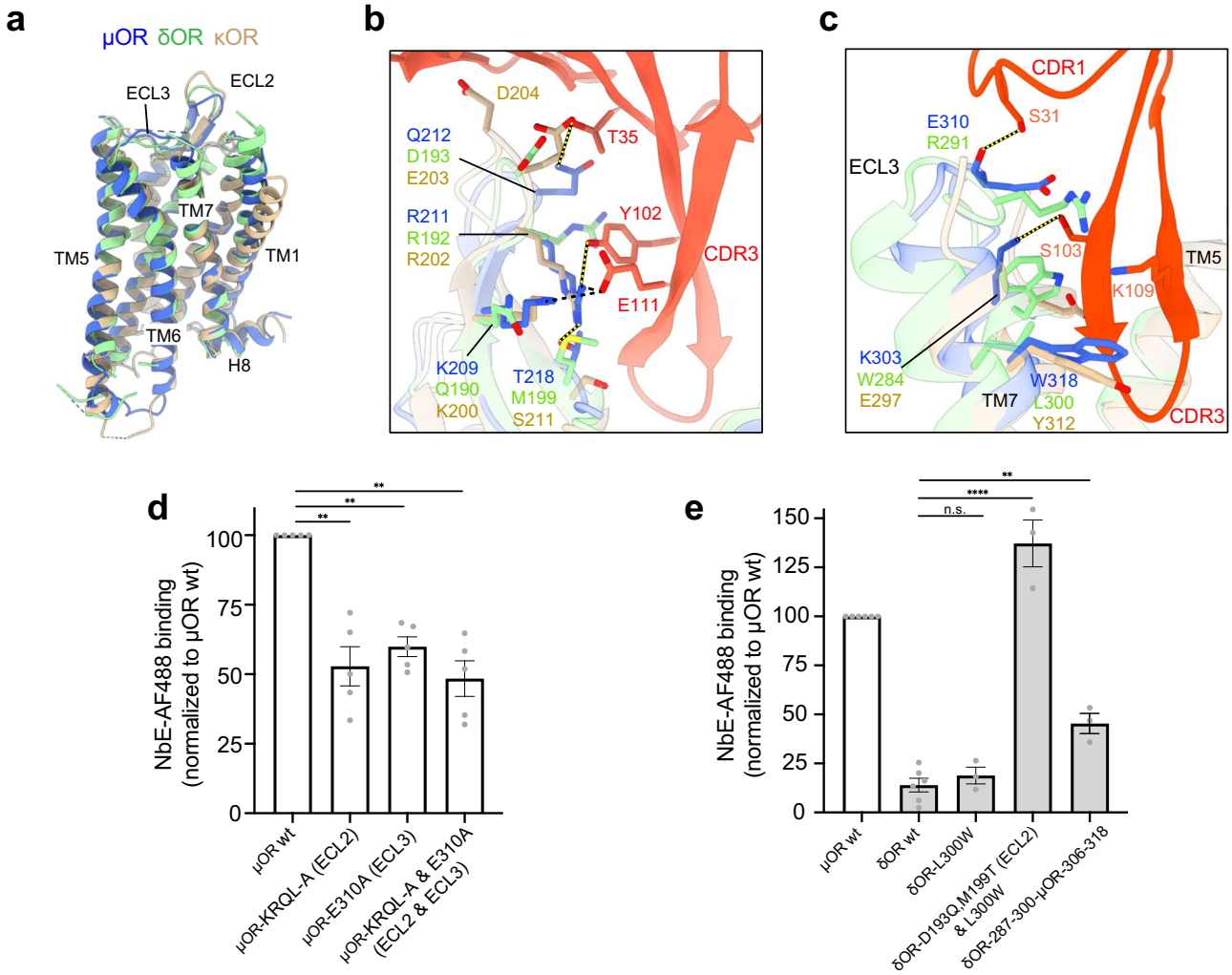

Fig. 4 | ECL regions confer NbE binding selectivity. a Superposition of the inactive state of the NbE-bound μOR (blue), inactive δOR (green, PDB: 4EJ4), and inactive κOR (brown, PDB: 4DJH) with ECL2 and ECL3 indicated. **b** Binding interface of different ECL2 regions (murine μOR, murine δOR, and human κOR) with NbE. For comparison, the δOR and κOR have been superimposed onto the μOR. $Q212^{ECL2}$ is unique to the μOR. **c** Binding interface of TM7 and ECL3 regions from the μOR, δOR, and κOR with NbE. For comparison, the δOR and κOR have been superimposed onto the TM7 and ECL3 regions of the μOR. Most interface residues differ between the different receptor subtypes. Color-coded as in (**a**). **d** NbE binding to the cells expressing wild-type (wt) μOR and ECL mutants (gated for similar receptor surface levels using anti-FLAG M1-AF647). NbE binding to wt μOR was normalized to 100%. μOR-KRQL-A mutant: K209, R211, Q212 and L219 substituted by alanine, E310A mutant: E310 substituted by alanine. μOR-KRQL-A & E310A: both sets of mutations combined. N = 5, mean ± SEM. $^{**}P = 0.0012$ (ECL2), 0.0047 (ECL3), 0.0010 (ECL2&3) by ordinary one-way ANOVA. **e** NbE binding to cells expressing δOR mutants (gated for similar receptor surface levels using anti-FLAG M1-AF647). NbE binding to wt μOR was normalized to 100%. The three δOR mutants include $δOR\ L300W^{7.35}$, a triple $δOR^{D193Q,\ M199T,\ L300W}$ mutant, and a δOR mutant with the entire ECL3 and distal parts of TM7 substituted by μOR residues ($δOR^{287\text{-}300\text{-}μOR\text{-}306\text{-}318}$). δOR wt: $N = 5$, δOR mutants: $N = 3$, mean ± SEM. $^{**}P = 0.0011$, $^{****}P = < 0.0001$, n.s. = 0.8998 by ordinary one-way ANOVA. In all panels, N indicates the number of independent experiments. Source data are provided as a Source Data file.

Extracellular loops confer NbE binding selectivity

To provide a rationale for NbE's selectivity for μOR over other OR family members (Fig. 1a, b), we focused our structural analyses on the extracellular loops, which represent the most variable regions in the OR family. In particular, ECL2 shows variations in sequence and length between the receptors (Fig. 4a and Supplementary Fig. 8), providing a possible explanation for the observed μOR selectivity given the specific interactions of NbE with ECL2 and ECL3 (Fig. 3c, d). $K209^{ECL2}$, $R211^{ECL2}$ and $Q212^{ECL2}$ interact with $E111^{NbE}$, $Y102^{NbE}$, and $T35^{NbE}$ respectively, thereby contributing to high-affinity binding (Fig. 4b and Supplementary Fig. 5b). Importantly, $Q212^{ECL2}$ is unique to the μOR. The centered $L219^{ECL2}$ of ECL2 stacks onto $Y108^{NbE}$ of CDR3 (Fig. 3b, c). $K303^{6.58}$, also unique to μOR, forms a specific hydrogen bond with $S103^{NbE}$ that likely stabilizes ECL3 in a conformation that allows several nonspecific side chain-main chain interactions between μOR and NbE, with $E310^{ECL3}$ being at ECL3's center (Fig. 4c and Supplementary Fig. 5b). Binding of NbE to μOR induces clear shifts for ECL2, parts of TM6, ECL3 and TM7 compared to the other two antagonist-bound μOR structures (Supplementary Fig. 6a).

To probe the relevance of μOR's ECLs in NbE binding, we first substituted ECL2 residues $K209^{ECL2}$, $R211^{ECL2}$, $Q212^{ECL2}$ and $L219^{ECL2}$ ('KRQL' motif) by alanine and tested NbE binding to the μOR mutant by flow cytometry, gating for cells with similar μOR surface expression (Supplementary Fig. 9a, b). Compared to wild-type μOR, the KRQL-A mutant showed 50% reduced NbE binding, indicating a lower affinity for the ECL2 mutant (Fig. 4d). Exchanging $E310^{ECL3}$ in ECL3 with alanine also significantly reduced NbE binding (Fig. 4d). Combining both the ECL2 and ECL3 mutations did not lead to further reduction in NbE binding, highlighting the central role of the orthosteric pocket interactions (Fig. 4d). All mutants retained comparable responses to DAMGO, as assessed by flow cytometry assays evaluating DAMGO-induced μOR internalization (Supplementary Fig. 9c).

Next, we reasoned that assimilating the δOR to the μOR, based on the uncovered interaction interfaces, might transform the δOR from a non-binder to a NbE binder. Given the established role of the amino acid position 7.35 in opioid receptor subtype selectivity[36,37], we first mutated δOR's $L300^{7.35}$ in the orthosteric pocket to the corresponding μOR residue $W318^{7.35}$ (δOR^{L300W} mutant). We then also converted the δOR residues $D193^{ECL2}$ (corresponds to μOR $Q212^{ECL2}$) and $M199^{ECL2}$ (corresponds to μOR $T218^{ECL2}$) into glutamine and threonine residues respectively (Fig. 4b, c). $T218^{ECL2}$ of μOR forms an intramolecular hydrogen bond with the guanidinium group of $R211^{ECL2}$. As a consequence of this loop stabilization, $K209^{ECL2}$ and $R211^{ECL2}$ of the μOR are ideally positioned to create the aforementioned hydrogen bond and salt bridge network with $Y102^{NbE}$ and $E111^{NbE}$ of NbE (Fig. 4b). Because $T218^{ECL2}$ is unique to the μOR, we speculated that mutating δOR $M199^{ECL2}$ into threonine might stabilize the ECL2 of the δOR in a conformation that favors NbE binding. We quantified fluorescent NbE binding to cells expressing μOR (control), wild-type δOR, or δOR mutants by flow cytometry in cells gated for similar receptor levels (Supplementary Fig. 9d). As expected, only non-specific background NbE binding was detected for cells expressing wild-type δOR (Fig. 4e). The NbE signal was not increased for cells expressing δOR^{L300W}. However, strong NbE binding was observed when cells expressed the triple mutant $\delta OR^{D193Q,\ M199T,\ L300W}$ (Fig. 4e). The results show that mutating two residues in the $ECL2^{\delta OR}$, combined with the orthosteric L300W mutation, can convert the non-binding δOR into a strong NbE binder. To test the role of ECL3, we next substituted the entire ECL3 as well as residues of the connecting α-helix 7 of the δOR (residues 287–300) with residues of the μOR (306-318). The substitution led to a moderate but significant increase in NbE binding (Fig. 4e), indicating that μOR's ECL3 region partially contributes to NbE binding.

In sum, the mutational and gain-of-function studies identify ECL2 and ECL3 as important contributors to NbE binding and receptor subtype selectivity.

Constrained peptide mimetics of NbE's CDR3 efficiently antagonize μOR

The centering of key contacts on a single CDR makes NbE's CDR3 a promising starting point for the design of ligands that downsize the Nb towards smaller peptides based on the antigen-binding paratope[38]. First, we designed and synthesized a library of linear peptides of increasing length, with the shortest peptide based on the four residues ^{105}SYFY^{108} that compose the β-turn segment at the tip of NbE's CDR3 (Fig. 5a). We systematically extended each peptide by one *N*- and one *C*-terminal residue of the $CDR3^{NbE}$ with the longest linear peptide spanning the 14 residues ^{100}KYYSGSYFYKSEYD^{113} (Fig. 5a). Peptide binding to μOR was assessed using the HTRF Tag-lite binding assay, which relies on fluorescence resonance energy transfer (FRET) between SNAP-tagged μOR labeled with terbium cryptate as FRET donor, and the red fluorescent opioid ligand naltrexone, serving as acceptor, with a decrease in FRET indicating competitive binding of a test compound. Binding of the control ligand naloxone and of NbE was readily detected with Ki values of 1.9 nM and 18 nM respectively (Fig. 5b and Supplementary Fig. 10a). In the Tag-lite binding assay, we detected significant binding of peptides 5 (12 residues) and 6 (14 residues) at Ki values of 1.3 μM and 3.1 μM, respectively, while the shorter peptides 1–4 showed little to no binding (Fig. 5b and Supplementary Fig. 10a, b).

Linear peptides are intrinsically flexible molecules able to adopt multiple conformations, which commonly deviate from ordered secondary structures, such as β-hairpins. This was confirmed by circular dichroism (CD), showing predominantly random coil CD spectra for peptides 1-6 in water and in the α-helix stabilizing solvent TFE (2,2,2-trifluoroethanol) (Supplementary Fig. 10c, e). To mimic the more rigid CDR3 β-hairpin structure observed in NbE, cyclic peptides 7 and 8 were designed. Here, the longest loop sequences (i.e., peptides 5 and 6, respectively) were grafted on the β-turn-inducing D-Pro-L-Pro dipeptide[39]. The position of the scaffold in these sequences was chosen to create a conformational bias for the observed hydrogen bonds in the NbE CDR3 β-hairpin structure, comparable to the conformational rigidity imposed by the Nb framework (Fig. 5a, c). CD measurements confirmed the beneficial effect of cyclization, as typical CD spectra for a β-hairpin structure were observed for cyclic peptide 8 (Supplementary Fig. 10d, f). The increased tendency of cyclic peptides 7 and 8 to adopt a β-hairpin structure compared to the linear peptides, as imposed by their design, also resulted in higher affinities for the μOR with Ki values of 245 nM and 39 nM, respectively, with the latter closely approaching the parental NbE affinity (Ki 18 nM) (Fig. 5d and Supplementary Fig. 10a). Consequently, this CDR3 peptidomimetic recapitulates closely the binding properties of the parental Nb. Previous work on such mimetics already delivered proof-of-concept, but never with equivalent binding properties[40,41].

Next, we tested whether the peptide mimetics retain the μOR-selective antagonism observed for NbE. Peptides 5 to 8 caused a concentration-dependent decrease in DAMGO-driven μOR signaling, with peptides 7 and 8 fully reversing μOR-mediated inhibition of cAMP production at high concentrations (Fig. 5e). Furthermore, DPDPE-driven δOR signaling was not antagonized by the peptides, showing that the CDR3 analogs retain receptor subtype selectivity (Fig. 5f). Taken together, the extensive interaction interface between the CDR3 of NbE and the μOR allowed the design of downsized linear and cyclic peptide mimetics that retain high-affinity μOR binding and antagonism. The NbE-based paratope mimetics provide a distinct source of small peptide opioid ligands and demonstrate the value of Nbs for biologics-based drug development.

Discussion

The emergence of biologics as therapeutic agents has opened new avenues in GPCR drug discovery[4]. In this study, we present an in-depth molecular characterization of the single-domain antibody fragment NbE that functionally interacts with the μOR. NbE selectively binds to the extracellular domains of μOR with nanomolar affinity and antagonizes its function. The cryo-EM structure of the NbE-μOR complex shows that NbE stabilizes the μOR in an inactive conformation that resembles μOR structures bound to the small molecule antagonists β-FNA or alvimopan[11,27]. Yet NbE exerts distinct effects on key residues in the orthosteric binding pocket as well as the extracellular regions of μOR. The interactions of NbE with μOR's ECL2 and ECL3 critically contribute to selective binding, paralleling recent observations for the role of extracellular vestibules in serving as selectivity filters of ORs for different opioid peptide agonists[30]. NbE exhibits an unprecedented ligand interaction profile with the μOR, centering almost all contacts on a hairpin loop formed by CDR3. The work opens the possibility to therapeutically target μOR with a biologic and provides an important structural template for new ligand design.

NbE's binding kinetics are characterized by a relatively slow on-rate and by nearly irreversible binding on the time scale studied, pointing to unique biomolecular recognition. Based on the conformational differences that we detect in NbE's unbound and μOR-bound state, in particular with regards to CDR3, it is possible that μOR binding drives NbE towards a conformation that is more complementary to the orthosteric pocket. Moreover, since GPCRs are known to be inherently dynamic and sample an ensemble of conformations in the unliganded state, NbE's slow on-rate may also reflect conformational selection of a weakly populated μOR conformation. The slow off-rate makes NbE a unique μOR ligand, holding the potential for long-lasting μOR-specific antagonism and distinct physiological effects. Underlining the therapeutic potential of pseudo-irreversible ligands, the small molecule antagonist methocinnamix, which very slowly dissociates from the μOR but shows rapid reversal at δOR and κOR[42], was recently shown to persistently attenuate the effect of opioid drugs for days to weeks following a single administration in animal

https://doi.org/10.1038/s41467-024-52947-6

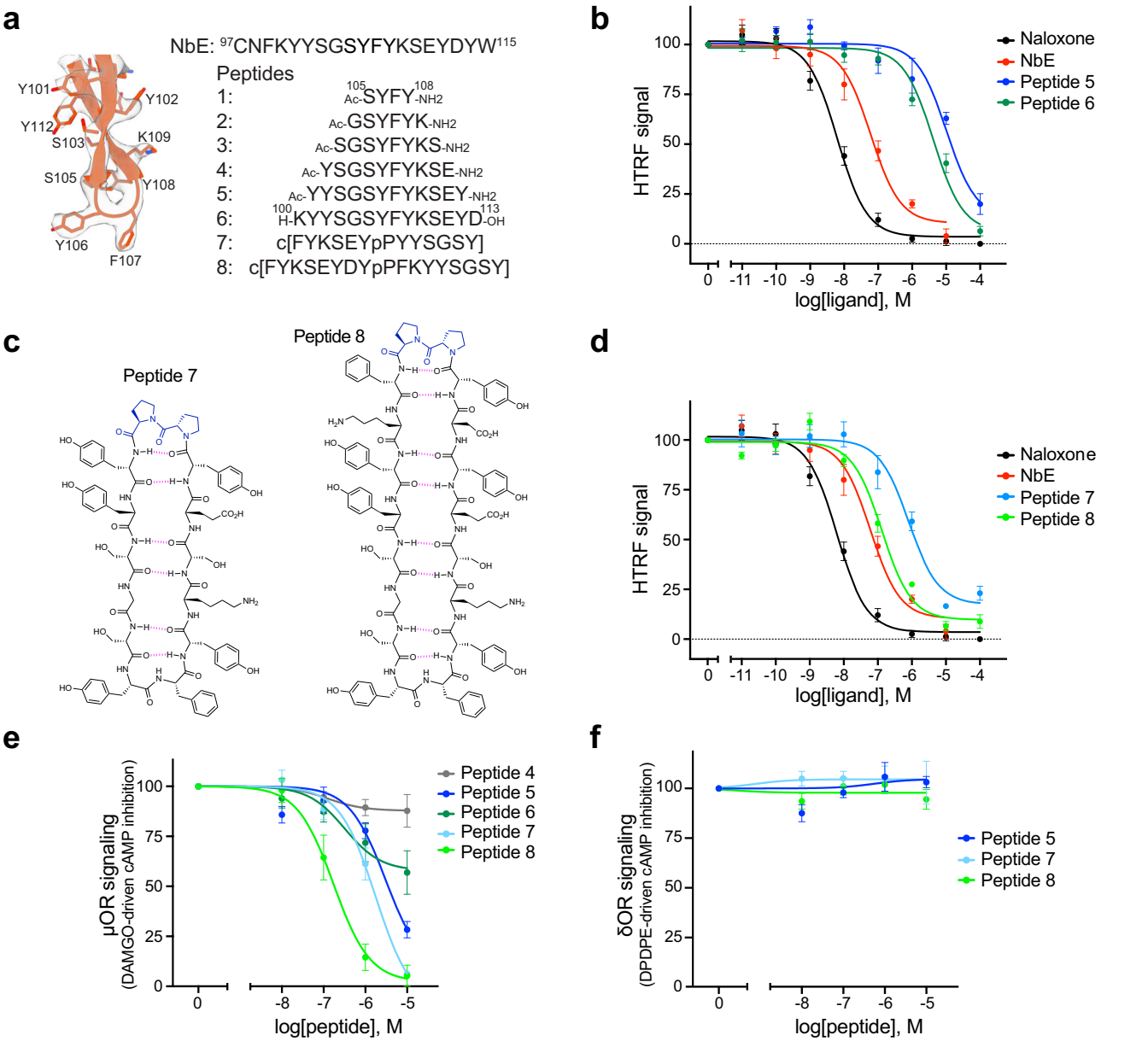

Fig. 5 | CDR3-based peptide-mimetics exhibit μOR binding and antagonism. **a** CDR3 conformation of NbE when bound to μOR (left), and peptides synthesized based on $CDR3^{NbE}$. Peptides 1 to 5 are *N*-acetylated, *C*-terminal carboxamides, peptide 6 is an unacetylated *C*-terminal carboxylic acid for improved solubility. Cyclic peptides 7 and 8 are grafted on the β-turn-inducing D-Pro-L-Pro scaffold. **b** HTRF competition binding assay profiles of naloxone and NbE (both $N = 11$), peptide 5 ($N = 3$), and peptide 6 ($N = 7$). Binding to HEK293 cells stably expressing SNAP-μOR, labeled with SNAP-Lumi4-Tb, and incubated with 3 nM red-labeled naltrexone derivative. Data normalized to cells without red-labeled naltrexone, mean ± SEM. **c** Chemical structures of cyclic peptides 7 and 8, with the D-Pro-L-Pro motif colored in blue and anticipated hydrogen bonds in pink. **d** HTRF competition binding assay profiles of naloxone and NbE (same data as in **b**), and peptides 7 and 8; $N = 3$, mean ± SEM. **e** Reversal of DAMGO-driven inhibition of cAMP accumulation. HEK293 cells stably expressing μOR and treated with 2.5 μM FSK and 10 nM DAMGO = 100% μOR signaling, cells only treated with FSK = 0% μOR signaling. All peptide conditions treated with 10 nM DAMGO and pre-incubated with increasing concentrations of peptides 4–8, $N = 4$, mean ± SEM. **f** Reversal of DPDPE-driven inhibition of cAMP accumulation. HEK293 cells stably expressing δOR and treated with 2.5 μM FSK and 1 nM DPDPE = 100% δOR signaling, cells only treated with FSK = 0% δOR signaling. All peptide conditions treated with 1 nM DPDPE and pre-incubated with increasing concentrations of peptides 5, 7, and 8, $N = 3$, mean ± SEM. In all panels, N indicates the number of independent experiments. Source data are provided as a Source Data files.

models[43,44]. Therefore, antagonists with a slow-off rate have therapeutic potential in the long-term treatment of opioid use disorders.

Recent structures of class A GPCRs bound to extracellular Nbs begin to reveal the diversity in Nb-driven GPCR modulation (Supplementary Fig. 11). For example, Nbs targeting the α1A-adrenergic receptor[45], rhodopsin[18], or orexin receptor 2[46] interact with extracellular loops and allosterically modulate receptor function without directly contacting the orthosteric pocket. In contrast, extracellular Nbs of the apelin receptor (APJ)[17] or the angiotensin II type 1 receptor (AT1R)[19] occupy the orthosteric pocket and mimic the binding of a peptide ligand. Similar to the NbE-μOR interaction, the APJ and AT1R Nbs access the orthosteric pocket via their long CDR3 loops. Yet APJ and AT1R Nbs both exhibit extensive additional interactions via CDR1 and CDR2, which contrasts with the limited interactions outside the CDR3 region detected for NbE. We find that linear and cyclic CDR3 peptide analogs retain biological activity and are selective for the μOR,

confirming the importance of the CDR3 sequence in NbE binding and, more broadly, demonstrating that CDR paratopes of Nbs can spur the development of low molecular weight antibody mimetics. Until now, OR peptide antagonists have been developed through structural modification and conversion of natural agonist peptides or by functional screening of synthetic short peptide libraries, often yielding peptides with limited OR subtype selectivity or reduced affinity[47–49]. The functional NbE-derived peptides described here comprise the NbE CDR3 residues that interact with the orthosteric pocket and include flanking Y102 and E111 that interact with μOR's ECL2, providing a rationale for their μOR selectivity. As expected, taking NbE's CDR3 sequence out of the rigid Nb framework resulted in a drop in affinity and potency. This effect could be compensated by conformational rigidification through cyclization with a β-hairpin stabilizing template, thereby functionally mimicking the parental NbE. Future steps towards fine-tuning the three-dimensional peptide structure will very likely give access to further improved binding and antagonist potency.

Beyond NbE's action as an extracellular ligand, we present a strategy to employ NbE when ectopically expressed in cells to modulate OR activity, which is broadly applicable to other GPCR-modulatory Nbs. Linkage of NbE to a GPI-anchor effectively displays NbE on the extracellular plasma membrane leaflet of transfected cells and blocks OR function, implementing a promising strategy to inhibit μOR in individual neurons. In the future, NbE can be fused with subcellular targeting motifs to achieve μOR inhibition at sub neuronal compartments, which would deliver high-precision genetically encoded modulators to untangle μOR signaling promoted by endogenous and exogenous ligands in functional studies in vitro and in vivo.

In sum, the present results reinforce the emerging notion that Nbs can uniquely engage with clinically important target proteins and constitute a new class of GPCR ligands. Mechanistic insights into Nb-GPCR engagement can instruct novel targeting strategies poised to impact future drug development.

Methods

Mammalian cell culture conditions and plasmids

HEK293 cells (CRL-1573, ATCC, female) were cultured in Dulbecco's modified Eagle's medium (DMEM, Gibco), supplemented with 10% fetal bovine serum (FBS, Thermo Fisher). HEK293 cells stably expressing *N*-terminally signal sequence FLAG (ssf)-tagged murine μOR (HEK293-μOR) were cultured in the presence of 250 μg/ml Geneticin (Gibco)[14]. A clonal HEK293 cell line stably expressing *N*-terminal signal sequence (ss) SNAP-tagged murine μOR was generated by cloning a 'CAG promoter, ssSNAP-μOR, RGK promoter, PuroR' cassette into a piggyBac transposon plasmid (Addgene #84239), co-transfection of the plasmid with piggyBac transposase, followed by puromycin selection and isolating single cell clones by FACS. For transient DNA expression, Lipofectamine 2000 (Invitrogen) was used according to the manufacturer's instructions. Published plasmids used in this study: Murine ssf-δOR, ssf-μOR, ssf-κOR, and ssf-NOPR in pcDNA3.1, NbE-6xHis in pXAP100[9], LgBiT-β-arrestin2 (human) in pNBe3[50], μOR-SmBiT (mouse), and miniGi1-LgBiT in pcDNA3.1[51]. Plasmids generated in this study: mNbE (N45K, Q117K, Q120P)-6xHis in pXAP100, GPI-anchored constructs: NbE and non-targeting Nb-ctr (NbALFA[52]) fused with a C-terminal GPI signal peptide from CD59, separated by a 15 aa (GGGGS)3 flexible linker, with N-terminal IL-2 secretory signal peptide and HA- or mRuby2-tag in pcDNA3.1. Mutant versions of murine ssf-μOR and ssf-δOR, and human ssf-μOR and ssf-δOR in pcDNA3.1. Plasmids were generated by In-Fusion cloning (Takara) or QuikChange Site-Directed Mutagenesis (Agilent). Plasmid sequences are available in the Yareta data repository (see Data Availability paragraph).

NbE purification and labeling

Escherichia coli WK6 cells were transformed with NbE (originally named 'Nb35'[9]) cloned into the pXAP100 plasmid, containing an *N*-terminal pelB signal sequence for periplasmic expression and *C*-terminal 6xHis-tag for purification. A single colony was grown in Terrific Broth media (1.2% w/v tryptone, 2.4% w/v yeast extract, 0.6% glycerol, 0.1% w/v glucose, 2 mM $MgCl_2$) at 37 °C with 50 μg/mL ampicillin to an optical density (OD A_{600}) of 0.7, followed by induction with 1 mM isopropyl β-D-1-thiogalactopyranoside (IPTG) and incubated overnight at 37 °C at 180 rpm shaking. Cell pellets were resuspended in TES buffer (0.2 M Tris, 5 mM EDTA, 0.5 M sucrose, pH 8.0) equivalent to 5% of bacterial culture volume, and kept on a shaker at 4 °C for at least 60 min. Cells underwent osmotic shock by adding double the volume of TES diluted 1:4 with H_2O and kept on the 4 °C shaker for 45 min. Cells were pelleted and discarded, and NbE contained in periplasmic lysate purified by Ni^{2+}-affinity (HisPur Ni NTA Resin; Thermo Fisher Scientific, catalog no. 88221) and eluted by low pH by adding acetate buffer (50 mM NaAc,1 M NaCl, pH 4.5-4.7) and immediately adding 1 M Tris (pH 7.5) to the eluates. NbE was further purified by size-exclusion chromatography (Superdex 75, Cytiva) and purity assessed by SDS-PAGE gel electrophoresis and gel staining with Coomassie blue (Bio-Rad, catalog no. 1610400). NbE was covalently conjugated at primary amines of lysines with Alexa Fluor 488 (Invitrogen, catalog no. A10235). For conjugation, 1 mg NbE was incubated with AF488 for 1 h at room temperature (RT) and NbE-AF488 separated from free dye using gel filtration. The concentration and degree of labeling was determined with a NanoDrop spectrophotometer (Thermo Scientific) and NbE-AF488 subsequently used in fluorescence microscopy- and flow cytometry-based binding assays.

Flow cytometry-based binding assay

HEK293 cells were transiently transfected with ssf-tagged murine μOR, δOR, κOR, and NOPR or with μOR and δOR mutants. 24 h post transfection, cells were detached with PBS-EDTA and resuspended in ice-cold assay buffer (PBS, 1 mM Ca^{2+}, 0.5 mM Mg^{2+}) at 8 million live cells/ml. Cells were incubated for 30 min at RT with NbE-AF488 at various concentrations and 10 min anti-FLAG M1 antibody (Sigma- Aldrich, catalog no. F-3040) conjugated to Alexa Fluor 647 (Invitrogen, catalog no. A20173) (anti-FLAG M1-AF647). Cells were washed twice with PBS and resuspended in FACS buffer (PBS, 1 mM Ca^{2+}, 0.5 mM Mg^{2+}, BSA 0.5%). Flow cytometry was performed using a Beckman Colter CytoFLEX Flow Cytometer. Data were analyzed with FlowJoTM v10 software and cells were gated for i) singlets, ii) living cells, and iii) comparable receptor expression using the anti-FLAG M1-AF647 signal. Conditions were normalized to the AF488 signal from μOR wt-expressing cells treated with 10 μM (Fig. 1b) or 1 μM (Fig. 4d, e) NbE-AF488. To probe competitive binding with naloxone, HEK293 cells stably expressing μOR were seeded at 5×10^4 live cells/cm^2 density. Cells were detached and resuspended in ice-cold assay buffer. Cells were then pre-treated with different concentrations of naloxone (Sigma-Aldrich, N7758) for 5 min, followed by addition of 1 μM NbE-AF488 for 30 min. Cells were washed twice with PBS, resuspended in FACS buffer, and analyzed using the Beckman Colter CytoFLEX Flow Cytometer. Data were analyzed with FlowJoTM v10 software and cells were gated for i) singlets and ii) living cells. Conditions were normalized to the maximum AF488 signal from the cells treated with 1 μM NbE-AF488 without addition of naloxone. The analyzed data was plotted using GraphPad Prism Version 9.2 software.

Luminescence-based cAMP assay

HEK293-μOR cells were transfected with a plasmid encoding pGloSensor-20F cAMP reporter (Promega). Cells were harvested 24 h post transfection and resuspended at a 1.5×10^6 live cells/ml in assay media (DMEM without phenol red or FluoroBrite DMEM, 250 μg/ml luciferin). 100 μl cell suspension was plated into each well of a clear bottom 96-well plate, and equilibrated for 60 min at 37 °C. To probe the reversal of 10 nM DAMGO (Sigma-Aldrich, E7384) or 30 nM morphine (morphine HCl, Sintetica) (concentrations correspond to their

respective EC50 values in the assay, agonist stock in H_2O, diluted in assay media), cells were pre-incubated for 15 min with NbE at different concentrations. Before addition of ligands, sequential luminescence images were collected to obtain baseline luminescence values using the FDSS/μCELL kinetic plate imager (Hamamatsu) with an integrated simultaneous dispensing head and simultaneous detection across the plate or using the Hidex Sense microplate reader. Cells were then treated with ligands and 2.5 μM Forskolin (FSK, Sigma-Aldrich, catalog no. F6886), followed by continuous luminescence imaging for 10 min, using two technical replicates per condition. Luminescence signals from cells not stimulated with FSK were considered as background and subtracted from all experimental conditions. The difference in luminescence signal between the baseline (average luminescence before addition of drugs (FDSS) or at beginning of acquisition (Hidex)) and the maximum signal in each condition was determined, and cells treated with 2.5 μM FSK (no agonist or NbE) normalized to 100%. To illustrate data on peptide-driven reversal of the DAMGO or DPDPE effect, the inhibition mediated by 10 nM DAMGO or 1 nM DPDPE in the absence of peptides was normalized as 100% μOR or 100% δOR signaling. GraphPad Prism Version 9.2 software was used for data analysis, statistical tests and graph plotting.

Split NanoLuc-based recruitment assay

HEK293 cells were seeded into 6-well plates and wells were transfected with 0.25 μg of μOR-SmBiT and (i) 0.25 μg of miniGi1-LgBiT or (ii) 0.25 μg of LgBiT-β-arrestin2 using 3 μl of Lipofectamine 2000. 24 h after transfection, cells were seeded into black, clear-bottom 384-well plates (20,000 cells per well) in assay media (FluoroBrite DMEM and the NanoLuc substrate NanoGlo (Promega, catalog no. N2012)), and incubated for 45 min at 37 °C. Cells were pre-incubated with different concentrations of NbE. Luminescence was recorded using the FDSS/μCELL kinetic plate imager (Hamamatsu) with an integrated simultaneous dispensing head and simultaneous detection across the plate. After acquiring baseline luminescence for 3 min, DAMGO (100 nM for miniGi1 and 1 μM for β-arrestin2 recruitment) was added to cells followed by continuous luminescence imaging for 10 min, using two technical replicates per condition. Luminescence signals from cells without any treatment were considered as background and subtracted from all experimental conditions. The difference in luminescence signal between the baseline (average luminescence before addition of DAMGO) and the maximum signal in each condition was determined, and cells treated with only DAMGO (no NbE) were normalized to 100%. GraphPad Prism Version 9.2 software was used for data analysis and graph plotting.

Confocal microscopy-based live cell binding assay

HEK293 cells were seeded on poly-L-lysine-coated 35-mm Cellvis glass-bottomed dishes (IBL, catalog no. 220.110.022) and, after 24 h, transfected with mouse ssf-μOR, -δOR, -κOR, or -NOPR (0.8 μg DNA) using 3 μl of Lipofectamine 2000. 16 to 24 h after transfection, cells were incubated at 37 °C with 1 μM NbE-AF488 for 30 min and anti-FLAG M1-AF647 antibody (1:1000 dilution) for 10 min in HBS imaging solution (Hepes-buffered saline with 135 mM NaCl, 5 mM KCl, 0.4 mM $MgCl_2$,1.8 mM $CaCl_2$, 20 mM Hepes, 1 mM d-glucose, 1% FBS, adjusted to pH 7.4). Cells were subsequently washed with PBS and imaged with a spinning disk confocal microscope (Nipkow, Zeiss) using Plan Apo 63x/1.4 Oil DICIII objective in a temperature and CO_2-controlled environment (37 °C, 5% CO_2).

Immunofluorescence and fixed cell binding assay

HEK293 cells were seeded onto 15-mm glass coverslips in 12-well plates and, after 24 h, transfected with human ssf-μOR or human ssf-δOR (0.4 μg of DNA using 1.5 μl of Lipofectamine 2000). 16 to 24 h after transfection, cells were treated with HA-tagged NbE for 30 min at 37 °C followed by washes with PBS and fixed using 4% formaldehyde (FA) in PBS. Cells were blocked with 1.5% BSA in PBS and incubated overnight at 4 °C with primary antibodies: HA-tag (6E2) mouse mAb (1:100 dilution; Cell Signaling Technology (CST), catalog no. 2367), Anti-FLAG rabbit (1:200 dilution; Merck Millipore Sigma, catalog no. F7425) in blocking solution. After three washes, cells were incubated with goat anti-rabbit immuno-globulin G (IgG) Alexa Fluor 647 (Thermo Fisher Scientific, catalog no. A32733) and goat anti-mouse IgG Alexa Fluor 568 (Thermo Fisher Scientific, catalog no. A11031) secondary antibodies (1:2000 dilution) for 45 min at RT. Samples were mounted using ProLong glass antifade mountant (Thermo Fisher Scientific, catalog no. P36982) and imaged with a spinning disk confocal microscope (Nipkow, Zeiss) using an Alpha Plan Apochromat 100x/1.46 Oil DIC. To check the localization of NbE-GPI constructs, HEK293 cells were seeded onto 15-mm glass coverslips in 12-well plates and, after 24 h, were transfected with NbE-GPI, 2xNbE-GPI, or Nb-ctr either fused to HA tag or the red fluorescent protein mRuby2. Cells were fixed using 4% FA in PBS. Cells were blocked with 1.5% BSA in PBS and incubated overnight at 4 °C with primary antibodies: mouse anti HA-tag conjugated with Alexa Fluor 488 (1:200, Life Technologies, catalog no. A-21287), and mouse anti-FLAG M1-647 (1:1000 dilution) to label the surface μOR. After three washes, cells were mounted using ProLong mountant and imaged with a spinning disk confocal microscope (Nipkow, Zeiss) using an Alpha Plan Apochromat 100x /1.46 Oil DIC.

Flow cytometry-based internalization assay

HEK293 cells were seeded onto 12 well-plate and transiently transfected with ssf-tagged murine wt μOR or μOR mutants. 24 h post transfection, cells were treated with 10 μM DAMGO or vehicle control for 25 min. Cells were immediately washed with ice-cold PBS, and surface receptors labeled for 10 min with anti-FLAG M1-AF647 (1:1000 dilution) at 4 °C. Cells were then resuspended in 500 μl FACS buffer (PBS, 1 mM Ca^{2+}, 0.5 mM Mg^{2+}, BSA 0.5%) and analyzed by flow cytometry (Beckman Colter Cytoflex). Data was analyzed with FlowJoTM v10 software and cells were gated for singlets and further gated for receptor expression. The area under curve (AUC) was calculated as a measure of the receptor level from the histogram of the gated population using the formula: AUC = sum of counts x width of the histogram bin; where the width of the bin was calculated using Sturges' formula. The receptor levels of the vehicle control (no DAMGO) was normalized to 100% for each condition and each experimental replicate.

Tag-lite HTRF binding assay

HEK293 cells stably expressing SNAP-μOR were labeled with 100 nM Tag-lite SNAP-Lumi4-Tb (Revvity, catalog no. SSNPTBC). Labeled cells were resuspended at a concentration of 1×10^6 cells/ml. 10 μl of the resuspension was plated in each well of low volume 96-well plates or 384-well plates to obtain 10'000 cells per well. 5 μl of labeled antagonist (Revvity, catalog no. L0005RED) was added to each well, resulting in a final ligand concentration of 3 nM, followed by addition of different concentrations of the test compound, and incubation for 3 h at RT, protected from light. Each experimental condition was performed in technical triplicates. Upon reaching equilibrium after 3 h, the FRET signal at 620 nm and 660 nm was read using a SpectraMax Paradigm Multi-Mode Microplate Reader (Molecular Devices). The ratio of the acceptor and donor emission signals (HTRF ratio signal) for each individual well was calculated. HTRF signals were plotted against concentrations. All conditions were normalized to the maximum HTRF ratio from the wells with 3 nM labeled reference antagonist (L0005RED). The signal from 1 μM naloxone condition was considered as background. GraphPad Prism Version 9.2 software was used for data analysis, statistical tests, and graph plotting.

Grating coupled interferometry assay

Grating coupled interferometry (GCI) experiments were conducted on a Creoptix WAVE delta system using 4PCP chips (Creoptix AG). The

chips were conditioned with 100 mM sodium borate (pH 9.5) and 1 M NaCl (Xantec). Neutravidin (100 µg/µl in 10 mM sodium acetate, pH 5.0) was immobilized on the chip surface using standard amine coupling. This included 420 s of surface activation with a 1:1 mix of 400 mM EDC and 100 mM NHS (Xantec), 420 s neutravidin injection, 420 s BSA (0.5%) injection, and a final 420 s surface passivation with 1 M ethanolamine at pH 8.0. Subsequently, biotin-NbE was captured at three concentrations: 100 µg/µl, 20 µg/µl, and 1 µg/µl, yielding surface masses of approximately 3700, 3500, and 2300 pg/mm², respectively. Any remaining neutravidin sites were filled with 100 µg/µl biotin-BSA. All preparation steps were performed at 10 µl/min flow rate. The analyte, containing purified µOR or the TCR-CD3 complex (negative control), was injected in a 1:2 dilution series from 7.8 nM to 1000 nM at 45 µl/min. The running buffer contained 25 mM HEPES (pH 7.5), 100 mM NaCl, 0.01% LMNG, and 0.001% CHS. Blank injections and a reference channel were used for double referencing, and a 0-2% dimethylsulfoxide (DMSO) calibration curve was employed for bulk refractive index correction. Data were analyzed with Creoptix WAVEcontrol software, with corrections made for X and Y offset, DMSO calibration, and double referencing. A 1:1 Langmuir binding model with bulk correction was used for all experiments. Consistent results were observed across the three NbE concentrations.

Purification of the anti-Fab Nb

A fragment encoding the anti-Fab nanobody[31] was synthesized by GeneArt (Thermo Fisher Scientific) and subsequently cloned into the pET28a vector downstream of a 6xHis tag. The resulting fusion proteins were expressed in *Escherichia coli* BL21 (DE3) at 18 °C overnight. Protein expression was induced with 0.5 mM IPTG at an OD A_{600} of 0.6. The fusion proteins were first purified in batch by a Ni^{2+}-affinity step (HisPur Ni-NTA Resin; Thermo Fisher Scientific), before being further purified by size-exclusion chromatography (Superdex 75 Increase 10/300 GL). The final protein buffer solution contained 25 mM Tris-HCl (pH 7.5) and 150 mM NaCl (no reducing agents). Monomeric anti-Fab nanobody fractions were pooled, concentrated to ~3.8 mg/ml, flash-frozen in liquid nitrogen, and stored at −70 °C.

Purification of the NabFab

The NabFab plasmid was kindly provided by the group of Prof. Kaspar Locher, ETH Zürich[31]. Chemically competent C43 *Escherichia coli* cells were used for protein expression. Four liters of TB autoinduction media (Terrific Broth containing 0.4% glycerol, 0.01% glucose, 0.02% lactose,1.25 mM $MgSO_4$ and 100 µg/ml ampicillin) were inoculated with overnight cultures from single colonies and incubated for 6 h at 37 °C, before shifting to 30 °C for expression overnight at 180 rpm shaking. Cells were resuspended in lysis buffer containing 50 mM Tris-HCl pH 7.5, 200 mM NaCl, protease inhibitor cocktail tablets (PIC) (complete EDTA-free, Roche Diagnostics) and 5 units/ml supernuclease (Novagen) and lysed by sonication. The lysate was incubated in a water bath at 65 °C for 40 min and spun down at 20,000x g for 30 min. The filtered supernatant was loaded on a HiTrap Protein L column (Cytiva), pre-equilibrated with 50 mM Tris-HCl (pH 7.5) and 500 mM NaCl. The protein was eluted using 0.1 M acetic acid and immediately loaded onto a Hitrap SP HP (Cytiva) column pre-equilibrated with buffer A (50 mM sodium acetate, pH 5.0). After a washing step, the NabFab was eluted using a salt gradient with buffer B (50 mM sodium acetate, 2 M NaCl, pH 5.0). The final protein buffer contained 25 mM Tris-HCl pH 7.5, 150 mM NaCl, the protein was concentrated to 7.0 mg/ml, flash-frozen and stored at −70 °C.

Purification of µOR

DNA coding for the full-length murine µOR was subcloned into the pF1 vector. The resulting construct comprises an N-terminal signal sequence, a Flag epitope tag and a C-terminal HRV-3C protease cleavage site followed by a Strep II tag and 8x His tag. µOR was expressed in Sf9 cells using baculoviruses in the presence of 10 µM naloxone. Typically, 20 ml of P3 viruses were used to infect 500 ml of Sf9 cells. Cells were infected at a cell density of roughly 3.0×10^6 cells/ml, incubated for 48 h at 27 °C at 110 rev/min and harvested by centrifugation at a cell viability of 80–85%. The purification of µOR has been previously described[27]. All purification steps were performed at 4 °C. Briefly, Sf9 cell pellets were lysed using hypotonic buffer containing 20 mM HEPES pH 7.5, 5 mM $MgCl_2$, PIC, 5 units/ml supernuclease, 10 µM naloxone (Sigma-Aldrich) and 2 mg/ml iodoacetamide (Sigma-Aldrich), and gently stirred for 1 h. Cell membranes were separated by ultracentrifugation at 100,000 × *g* for 40 min and resuspended in solubilization buffer made of 25 mM HEPES pH 7.5, 500 mM NaCl, 1% LMNG, 0.1% CHS, PIC, 10 µM naloxone and 2 mg/ml iodoacetamide using a Dounce homogenizer. The solution was gently stirred for 4 h. The insoluble debris was removed by ultracentrifugation at 100,000 × *g* for 1 h. The supernatant (supplemented with 20 mM imidazole) was incubated for 2-3 h with HisPur Ni-NTA Resin and extensively washed with wash buffer A (25 mM HEPES pH 7.5, 500 mM NaCl, 0.1% LMNG, 0.01% CHS, 1 µM naloxone, 10 mM imidazole), followed by buffer B (25 mM HEPES pH 7.5, 500 mM NaCl, 0.1% LMNG, 0.01% CHS, 1 µM naloxone, 10 mM $MgCl_2$, 10 mM ATP). Proteins were eluted using an imidazole gradient and subsequently loaded onto a 5 ml StrepTactin Superflow Cartridge (Qiagen) at a flow rate of 0.8 ml/min. The column was washed with wash buffer C (25 mM HEPES pH 7.5, 500 mM NaCl, 0.05% LMNG, 0.005% CHS) to remove contaminations and residual naloxone. µOR was eluted using 2.5 mM desthiobiotin. The µOR was further purified by size exclusion chromatography. A Superose 6 Increase 10/300 GL column (GE Healthcare Life Sciences) was pre-equilibrated with 20 mM HEPES pH 7.5, 100 mM NaCl, and 0.001% LMNG/0.0001% CHS. Fractions containing µOR were concentrated, flash-frozen, and stored at −80 °C.

Purification of the TCR-CD3 complex (control in GCI assay)

The two plasmids encoding the human TCRγδ and CD3γδε$_2$ζ$_2$ complex were transfected into the HEK293F cells. The cell pellets were subjected to repeated cycles of Dounce homogenization in hypoosmotic buffer (25 mM HEPES pH 7.5) supplemented with protease inhibitor cocktail (Roche). The cell membrane was homogenized in a solubilization buffer (25 mM HEPES pH 7.5, 500 mM NaCl, 1% LMNG, 0.1% CHS), and solubilized for 4 h in 4 °C. Cell debris and insoluble material was removed by centrifugation at 35,000 g for 30 min. The supernatant was gently mixed with strep-tactin resin at 4 °C overnight for binding. The resin was washed with buffer A (25 mM HEPES pH 7.5, 100 mM NaCl, 0.01% LMNG, 0.001% CHS), and eluted with buffer B (25 mM HEPES pH 7.5, 100 mM NaCl, 0.01% LMNG, 0.001% CHS, 50 mM biotin). The eluted sample underwent gel filtration using a Superose 6 Increase 10/300 GL column in buffer (25 mM HEPES, pH 7.5, 100 mM NaCl, 0.01% LMNG, 0.001% CHS) and was concentrated to around 1 mg/ml.

NbE-µOR-Fab module complex assembly

To assemble the NbE-µOR-Fab module complex, freshly prepared µOR was incubated with mNbE (containing framework mutations N45K, Q117K, Q120P to enable NabFab binding[31]), NabFab and anti-Fab Nb in a molar ratio of 1:2:2.5:3 overnight, gently mixed at 4 °C. A final size-exclusion step using a Superose 6 Increase 10/300 GL column was conducted. Fractions containing the complex were pooled, concentrated to around 2.8 mg/ml and immediately used for EM grid preparation. The assembled complex was analyzed by application to a Superose 6 Increase 5/150 column.

Cryo-EM sample preparation and data collection

3 µl of freshly purified NbE-µOR-Fab module complex were applied onto holey gold grids (Quantifoil UltrAuFoil R1.2/1.3, 300 mesh), front blotted for 3–4 s with 1 mm additional movement (95% humidity at

15 °C) before being plunged into liquid ethane using an EM GP2 automatic plunge freezer (Leica). The cryo-EM data sets of NbE-μOR-Fab module complex were acquired on a Thermo Scientific Talos Arctica Cryo-TEM at an accelerating voltage of 200 kV. A total of 5'938 movies were recorded using a Falcon III direct electron detector at a nominal magnification of 150,000x, resulting in a pixel size of 0.9759 Å. Data were collected using EPU (Thermo Fisher Scientific) with one image per hole, a defocus range of −0.6 to −2.0 μm and a total electron dose of 40$e^-/Å^2$ distributed over 44 frames per acquisition. Data acquisition was monitored on-the-fly pre-processing using CryoSPARC v.3.3.1[53].

Cryo-EM image processing

All data were processed using CryoSPARC v.3.3.1 and RELION 3.1[53,54]. The data processing workflow is summarized in Supplementary Fig. 4. First, raw movies were aligned and dose-weighted using patch-based motion correction[55]. Contrast transfer function (CTF) parameters were estimated by patch-based CTF estimation[53]. Only micrographs with a CTF fit better than 4.0 Å resolution were selected for further processing, resulting in a set of 5'686 micrographs. Particles were initially picked using a blob picker with a minimum and maximum diameter of 70 Å and 200 Å, respectively. The resulting 2D classes were fed into the Topaz particle-picking pipeline to increase the number and accuracy of picked particles. After several rounds of 2D classification (and removal of duplicated particles) 704'786 particles were selected. Ab initio reconstruction with multiple classes was followed by heterogeneous refinement. The best class contained 509,809 particles. 3D classification helped to further clean up the particle set. 3D refinement using non-uniform refinement and CTF refinement (global and local CTF refinement) resulted in a reconstruction of 3.1 Å resolution. To further improve the density of the μOR, refined particles were imported into RELION 3.1 for 3D classification without alignment (K = 4 and T = 12), using a soft mask on the seven transmembrane helices of the μOR. The best class showing high resolution features was selected (445,766 particles) and particles were re-imported to CryoSPARC for non-uniform refinement followed by local refinement with a soft mask around the NbE-μOR. As a result, the density for the NbE-μOR interface was significantly improved. All maps were sharpened with deepEMhancer[56]. All resolution estimations were derived from Fourier shell correlation (FSC) calculations between reconstructions from two independently refined half-sets, and reported resolutions are based on the FSC = 0.143 criterion. Local resolution estimations are obtained by ResMap[57].

Cryo-EM model building and refinement

The crystal structure of inactive μOR bound to a covalent antagonist (PDB: 4DKL) was used as an initial reference[27]. Similarly, the crystal structure of the NbE published in this manuscript was used as an initial model. For NabFab and anti-Fab Nb, the cryo-EM structure of VcNorM complex was used as initial models[31]. All initial models were fitted into cryo-EM maps using Chimera X[58], then manually built in Coot[59], iteratively and real-space refined using PHENIX[60]. Model validation was performed with MolProbity[61]. Structural figures were generated in Chimera X[58].

Crystallization and data collection

Purified NbE was concentrated to ~30 mg/mL for crystallization. Crystals were grown using the hanging drop vapor diffusion method at 16 °C in a temperature-controlled incubator. The best NbE crystals grew in 1 M succinic acid pH 7.0, 1-2% polyethylene glycol 2000 monomethyl ether (PEG 2000 MME) and 0.1 M Hepes, pH 7.0, reaching their final size within 3 days. Crystals of NbE were cryoprotected using the well solution supplemented with 25% glycerol and flash frozen in liquid nitrogen. Diffraction data was collected at the Advanced Photon Source on beamline 23-IDD on a Pilatus 6 M detector. The final dataset was collected from a single crystal of NbE, with reflections extending to 2.85 Å resolution.

Crystallographic data processing and model refinement

Reflection data was integrated using XDS[62], and scaled and merged using Aimless as part of the CCP4 suite[63]. Initial phases were obtained using molecular replacement in Phaser[64], using a homology model from SwissModel[65] yielding three copies of NbE in the asymmetric unit. Iterative rounds of manual model building and automated refinement were carried out in Coot[66] and Phenix[60], respectively. The final model was refined to a R_{free} of 0.331 with favorable geometry (96% Ramachandran favored, 3% allowed, and 0.3% outliers). Of the three chains in the asymmetric unit, one (chain A) is characterized by exemplary density for the resolution and was used as an initial model for building of the NbE-μOR-Fab module complex.

Synthesis of linear peptides 1-6

Peptides were synthesized using Fmoc-based solid phase peptide synthesis (SPPS) on a microwave assisted peptide synthesizer (CEM Liberty Lite). The synthesis was performed on 0.1 mmol scale using preloaded Wang resin or Rink Amide resin depending on the desired *C*-terminal end of the peptide, being a carboxylic acid or carboxamide. Fmoc deprotection was performed at 90 °C for 3 min using a solution of 20% 4-methylpiperidine in *N,N*-dimethylformamide (DMF) during the entire synthesis. Each coupling was done using 5 equivalents of Fmoc-protected amino acid, with 0.5 M *N,N'*-diisopropylcarbodiimide (DIC) and 1 M Oxyma Pure as coupling reagents. *N*-terminal acetylation has been done manually using 10 equivalents of acetic anhydride and 5 equivalents of *N,N'*-diisopropylethylamine (DIPEA) during 1 h in DMF. After completion of the sequence, the resin was washed several times with dichloromethane (DCM), followed by the cleavage using a cocktail solution consisting of 90% trifluoroacetic acid (TFA), 5% triisopropylsilane and 5% ultrapure water during 4 h. After freeze-drying, crude peptides were obtained and purified using preparative HPLC. More specifically, a Gilson HPLC system, equipped with Gilson 322 pumps and a Supelco Discovery BIO Wide Pore C18 column (25 cm×21.2 mm, 10 μm), was used. Crude peptides were dissolved in DMSO and purified using linear gradients of water (containing 0.1% TFA) in acetonitrile (containing 0.1% TFA) at a flow rate of 20 mL min^{-1}. Finally, fractions were collected by UV detection at 214 nm, and the accompanying purities were assessed by analytical RP-HPLC using a Chromolith High Resolution C18 column (50 mm × 4.6 mm, 1.1 μm, 150 Å), after which the pure fractions with a purify exceeding 95% were combined and lyophilized to obtain the final purified peptide as a powder (TFA salt). The identity of the peptides was confirmed by High Resolution Mass Spectrometry (HRMS) on a Waters Synapt XS QTOF system with an Electron Spray inlet. Lock Mass correction was performed using a Leucine Enkephalin (100 μg $μL^{-1}$) solution in H_2O:MeCN (1:1) with 0.1% formic acid.

Synthesis of cyclic peptides 7 and 8

Peptides were manually synthesized using Fmoc/tBu-based SPPS as linear variants using polypropylene syringes equipped with a polyethene frit. The synthesis was performed on a 0.15 mmol scale using a 2-chlorotrityl chloride resin. Between every step, the resin was washed with DMF (3 times) and DCM (3 times). Loading of the resin (2 equiv) was performed overnight with the appropriate Fmoc/tBu-protected amino acid (1 equiv) and DIPEA (2 equiv) in dry DCM. Fmoc deprotections were performed using a solution of 20% 4-methylpiperidine in DMF for 5 and 15 min. Amino acid couplings were carried out using 4 equiv of protected amino acid, 4 equiv of *N,N,N',N'*-tetramethyl)-*O*-(1H-benzotriazol-1-yl)uronium hexafluorophosphate (HBTU) and 8 equiv of DIPEA in DMF for 1 to 3 h. After final Fmoc removal, the peptides were cleaved from the resin under their side chain-protected forms using a solution of 20% hexafluoro-2-propanol in DCM for 90 min. After evaporation under reduced pressure, a powder was obtained which was directly used for head-to-tail cyclization in solution. Cyclization of the linear, side-chain protected peptides was directly

performed on the crude peptides (0.05-0.1 mmol scales) using PyOxim (5 equiv), Oxyma Pure (1 equiv) and DIPEA (12 equiv) in DCM (0.5 mM). After 21 h the solvent was removed under reduced pressure, followed by removal of the side chain protecting groups using a mixture consisting of 90% trifluoroacetic acid, 5% triisopropylsilane and 5% ultrapure water for 90 min. After evaporation under reduced pressure, the peptides were precipitated and washed with cold diethyl ether. After freeze-drying, crude peptides were obtained and purified by preparative HPLC as described above for the linear peptides 1-6, using a ReproSil 100 C18 column (25 cm × 20 mm, 5 µm) at a flow rate of 15 mL min^{-1}. Peptides with a purity exceeding 95% were analyzed, characterized and obtained as described for the linear peptides 1-6.

Circular dichroism of linear and cyclic peptides 1-8

Circular dichroism spectra were recorded on an Applied Photophysics ChiraScanTM-plus spectrometer (ChiraScan v.4.5.1848.0) at 20 °C with nitrogen gas purging at 4 L/min. Measurements were performed in a quartz cuvette with a path length of 1 mm containing 100 µL of the peptide solutions. The spectral range of 300–180 nm was sampled with a 1 nm step size, 1 nm bandwidth and 1 s collection time per step. The background was subtracted for all spectra. Raw data was obtained in ellipticity θ (mdeg) and converted towards the mean residue molar ellipticity [θ] considering the number of amide bonds.

Reporting summary

Further information on research design is available in the Nature Portfolio Reporting Summary linked to this article.

Data availability

The EM maps of the NbE-µOR-Fab module complex have been deposited in the Electron Microscopy Data Bank (EMDB) under the accession code EMD-18541. Protein coordinates for NbE-µOR-Fab module complex structure and the crystal structure of the isolated nanobody NbE have been deposited in the Protein Data Bank (PDB) under accession codes 8QOT and 8V8K, respectively. The raw and analyzed experimental data are available in the Yareta repository [https://doi.org/10.26037/yareta:swsqivwptvga7g6yx5eb2zovqu]. Source data are provided with this paper.

References

1. Santos, R. et al. A comprehensive map of molecular drug targets. *Nat. Rev. Drug Discov.* **16**, 19–34 (2017).
2. Sriram, K. & Insel, P. A. G protein-coupled receptors as targets for approved drugs: how many targets and how many drugs? *Mol. Pharmacol.* **93**, 251–258 (2018).
3. Hauser, A. S., Attwood, M. M., Rask-Andersen, M., Schiöth, H. B. & Gloriam, D. E. Trends in GPCR drug discovery: new agents, targets and indications. *Nat. Rev. Drug Discov.* **16**, 829–842 (2017).
4. Hutchings, C. J., Koglin, M., Olson, W. C. & Marshall, F. H. Opportunities for therapeutic antibodies directed at G-protein-coupled receptors. *Nat. Rev. Drug Discov.* **16**, 661 (2017).
5. Laeremans, T. et al. Accelerating GPCR drug discovery with conformation-stabilizing VHHs. *Front Mol. Biosci.* **9**, 863099 (2022).
6. Jovčevska, I. & Muyldermans, S. The therapeutic potential of nanobodies. *BioDrugs* **34**, 11–26 (2020).
7. Manglik, A., Kobilka, B. K. & Steyaert, J. Nanobodies to study G protein-coupled receptor structure and function. *Annu. Rev. Pharmacol. Toxicol.* **57**, 19–37 (2017).
8. Heukers, R., De Groof, T. W. M. & Smit, M. J. Nanobodies detecting and modulating GPCRs outside in and inside out. *Curr. Opin. Cell Biol.* **57**, 115–122 (2019).
9. Huang, W. et al. Structural insights into µ-opioid receptor activation. *Nature* **524**, 315–321 (2015).
10. Rasmussen, S. G. F. et al. Structure of a nanobody-stabilized active state of the β(2) adrenoceptor. *Nature* **469**, 175–180 (2011).
11. Robertson, M. J. et al. Structure determination of inactive-state GPCRs with a universal nanobody. *Nat. Struct. Mol. Biol.* **29**, 1188–1195 (2022).
12. Kruse, A. C. et al. Activation and allosteric modulation of a muscarinic acetylcholine receptor. *Nature* **504**, 101–106 (2013).
13. Irannejad, R. et al. Conformational biosensors reveal GPCR signalling from endosomes. *Nature* **495**, 534–538 (2013).
14. Stoeber, M. et al. A genetically encoded biosensor reveals location bias of opioid drug action. *Neuron* **98**, 963–976.e5 (2018).
15. McMahon, C. et al. Synthetic nanobodies as angiotensin receptor blockers. *Proc. Natl Acad. Sci.* **117**, 20284–20291 (2020).
16. Scholler, P. et al. Allosteric nanobodies uncover a role of hippocampal mGlu2 receptor homodimers in contextual fear consolidation. *Nat. Commun.* **8**, 1967 (2017).
17. Ma, Y. et al. Structure-guided discovery of a single-domain antibody agonist against human apelin receptor. *Sci. Adv.* **6**, eaax7379 (2020).
18. Wu, A. et al. Structural basis for the allosteric modulation of rhodopsin by nanobody binding to its extracellular domain. *Nat. Commun.* **14**, 5209 (2023).
19. M. A. Skiba et al. Antibodies expand the scope of angiotensin receptor pharmacology. *Nat. Chem. Biol*. https://doi.org/10.1038/s41589-024-01620-6 (2024).
20. Schlimgen, R. R. et al. Structural basis for selectivity and antagonism in extracellular GPCR-nanobodies. *Nat. Commun.* **15**, 4611 (2024).
21. Corder, G., Castro, D. C., Bruchas, M. R. & Scherrer, G. Endogenous and exogenous opioids in pain. *Annu. Rev. Neurosci.* **41**, 453–473 (2018).
22. Kieffer, B. L. & Evans, C. J. Opioid receptors: from binding sites to visible molecules in vivo. *Neuropharmacology* **56**, 205–212 (2009).
23. Manglik, A. et al. Structure-based discovery of opioid analgesics with reduced side effects. *Nature* **537**, 185–190 (2016).
24. Faouzi, A. et al. Structure-based design of bitopic ligands for the µ-opioid receptor. *Nature* **613**, 767–774 (2023).
25. Wang, H. et al. Structure-based evolution of G protein-biased µ-opioid receptor agonists. *Angew. Chem. Int. Ed. Engl.* **61**, e202200269 (2022).
26. Volkow, N. D. & Collins, F. S. The role of science in addressing the opioid crisis. *N. Engl. J. Med.* **377**, 391–394 (2017).
27. Manglik, A. et al. Crystal structure of the µ-opioid receptor bound to a morphinan antagonist. *Nature* **485**, 321–326 (2012).
28. Zhuang, Y. et al. Molecular recognition of morphine and fentanyl by the human µ-opioid receptor. *Cell* **185**, 4361–4375.e19 (2022).
29. Koehl, A. et al. Structure of the µ-opioid receptor-Gi protein complex. *Nature* **558**, 547–552 (2018).
30. Wang, Y. et al. Structures of the entire human opioid receptor family. *Cell* **186**, 413–427.e17 (2023).
31. J. S. Bloch et al. Development of a universal nanobody-binding Fab module for fiducial-assisted cryo-EM studies of membrane proteins. *Proc. Natl. Acad. Sci. USA.* **118** (2021).
32. J. A. Ballesteros, H. Weinstein, "Integrated methods for the construction of three-dimensional models and computational probing of structure-function relations in G protein-coupled receptors" in *Methods in Neurosciences*, S. C. Sealfon, (ed). **25**, 366–428 (Academic Press, 1995).
33. Manglik, A. Molecular Basis of Opioid Action: From Structures to New Leads. *Biol. Psychiatry* **87**, 6–14 (2020).
34. Z. Li et al. Three-dimensional structural insights have revealed the distinct binding interactions of agonists, partial agonists, and antagonists with the µ opioid receptor. *Int. J. Mol. Sci.* **24**, 7042 (2023).
35. Chen, C. et al. Determination of the amino acid residue involved in [3H]beta-funaltrexamine covalent binding in the cloned rat mu-opioid receptor. *J. Biol. Chem.* **271**, 21422–21429 (1996).

36. Marie-Pepin, C., Yue, S. Y., Roberts, E., Wahlestedt, C. & Walker, P. Novel "restoration of function" mutagenesis strategy to identify amino acids of the δ-opioid receptor involved in ligand binding. *J. Biol. Chem.* **272**, 9260–9267 (1997).
37. Granier, S. et al. Structure of the δ-opioid receptor bound to naltrindole. *Nature* **485**, 400–404 (2012).
38. Van Holsbeeck, K., Martins, J. C. & Ballet, S. Downsizing antibodies: towards complementarity-determining region (CDR)-based peptide mimetics. *Bioorg. Chem.* **119**, 105563 (2022).
39. Obrecht, D., Chevalier, E., Moehle, K. & Robinson, J. A. β-Hairpin protein epitope mimetic technology in drug discovery. *Drug Discov. Today Technol.* **9**, e63–e49 (2012).
40. Van Holsbeeck, K. et al. Nanobody loop mimetics enhance son of sevenless 1-catalyzed nucleotide exchange on RAS. *Angew. Chem. Int. Ed. Engl.* **62**, e202219095 (2023).
41. Martin, C. et al. Rational design of Nanobody80 loop peptidomimetics: Towards biased β2 adrenergic receptor ligands. *Chemistry* **23**, 9632–9640 (2017).
42. Zamora, J. C. et al. Long-term antagonism and allosteric regulation of mu opioid receptors by the novel ligand, methocinnamox. *Pharmacol. Res. Perspect.* **9**, e00887 (2021).
43. Maguire, D. R. et al. Effects of acute and repeated treatment with methocinnamox, a mu opioid receptor antagonist, on fentanyl self-administration in rhesus monkeys. *Neuropsychopharmacology* **45**, 1986–1993 (2020).
44. Gerak, L. R. et al. Methocinnamox produces long-lasting antagonism of the behavioral effects of μ-opioid receptor agonists but not prolonged precipitated withdrawal in rats. *J. Pharmacol. Exp. Ther.* **371**, 507–516 (2019).
45. Toyoda, Y. et al. Structural basis of α1A-adrenergic receptor activation and recognition by an extracellular nanobody. *Nat. Commun.* **14**, 1–13 (2023).
46. Hong, C. et al. Structures of active-state orexin receptor 2 rationalize peptide and small-molecule agonist recognition and receptor activation. *Nat. Commun.* **12**, 815 (2021).
47. Dooley, C. T., Chung, N. N., Schiller, P. W. & Houghten, R. A. Acetalins: opioid receptor antagonists determined through the use of synthetic peptide combinatorial libraries. *Proc. Natl Acad. Sci. Usa.* **90**, 10811–10815 (1993).
48. Schiller, P. W. et al. Conversion of δ-, κ- and μ-receptor selective opioid peptide agonists into δ-, κ- and μ-selective antagonists. *Life Sci.* **73**, 691–698 (2003).
49. Purington, L. C., Pogozheva, I. D., Traynor, J. R. & Mosberg, H. I. Pentapeptides displaying μ opioid receptor agonist and δ opioid receptor partial agonist/antagonist properties. *J. Med. Chem.* **52**, 7724–7731 (2009).
50. Laschet, C., Dupuis, N. & Hanson, J. A dynamic and screening-compatible nanoluciferase-based complementation assay enables profiling of individual GPCR–G protein interactions. *J. Biol. Chem.* **294**, 4079–4090 (2019).
51. Radoux-Mergault, A., Oberhauser, L., Aureli, S., Gervasio, F. L. & Stoeber, M. Subcellular location defines GPCR signal transduction. *Sci. Adv.* **9**, eadf6059 (2023).
52. Götzke, H. et al. The ALFA-tag is a highly versatile tool for nanobody-based bioscience applications. *Nat. Commun.* **10**, 4403 (2019).
53. Punjani, A., Rubinstein, J. L., Fleet, D. J. & Brubaker, M. A. cryoSPARC: algorithms for rapid unsupervised cryo-EM structure determination. *Nat. Methods* **14**, 290–296 (2017).
54. J. Zivanov et al. New tools for automated high-resolution cryo-EM structure determination in RELION-3. *Elife* **7**, e42166 (2018).
55. Zheng, S. Q. et al. MotionCor2: anisotropic correction of beam-induced motion for improved cryo-electron microscopy. *Nat. Methods* **14**, 331–332 (2017).
56. Sanchez-Garcia, R. et al. DeepEMhancer: a deep learning solution for cryo-EM volume post-processing. *Commun. Biol.* **4**, 874 (2021).
57. Kucukelbir, A., Sigworth, F. J. & Tagare, H. D. Quantifying the local resolution of cryo-EM density maps. *Nat. Methods* **11**, 63–65 (2014).
58. Meng, E. C. et al. UCSF ChimeraX: Tools for structure building and analysis. *Protein Sci.* **32**, e4792 (2023).
59. Casañal, A., Lohkamp, B. & Emsley, P. Current developments in Coot for macromolecular model building of electron cryo-microscopy and crystallographic data. *Protein Sci.* **29**, 1069–1078 (2020).
60. Liebschner, D. et al. Macromolecular structure determination using X-rays, neutrons and electrons: recent developments in Phenix. *Acta Crystallogr D. Struct. Biol.* **75**, 861–877 (2019).
61. Williams, C. J. et al. MolProbity: more and better reference data for improved all-atom structure validation. *Protein Sci.* **27**, 293–315 (2018).
62. Kabsch, W. XDS. *Acta Crystallogr. D. Biol. Crystallogr.* **66**, 125–132 (2010).
63. Agirre, J. et al. The CCP4 suite: integrative software for macromolecular crystallography. *Acta Crystallogr D. Struct. Biol.* **79**, 449–461 (2023).
64. McCoy, A. J. Solving structures of protein complexes by molecular replacement with phaser. *Acta Crystallogr. D. Biol. Crystallogr.* **63**, 32–41 (2007).
65. Schwede, T., Kopp, J., Guex, N. & Peitsch, M. C. SWISS-MODEL: an automated protein homology-modeling server. *Nucleic Acids Res* **31**, 3381–3385 (2003).
66. Emsley, P. & Cowtan, K. Coot: model-building tools for molecular graphics. *Acta Crystallogr. D. Biol. Crystallogr.* **60**, 2126–2132 (2004).

Acknowledgements

We thank A. Radoux-Mergault for valuable discussions and M. de Lapeyrière for generating preliminary data on NbE's antagonism. We thank Y. Pfister for technical assistance, A. Howe for assistance with EM data collection at the DCI-Geneva (cryoGEnic) EM facility, the computing department for providing the infrastructure for cryo-EM analysis, N. Roggli for maintaining computing in the Molecular and Cellular Biology Department, and C. Bauer for his contributions to the cryoGEnic facility. W. Herrebout is acknowledged for kindly providing access to the CD spectrometer, and J. Bertouille is thanked for technical assistance. This work was supported by the Swiss National Science Foundation (PCEFP3_181282 to M.S. and 310030_185235 and TMSGI3_211581 to A.B.), the Helmut Horten Foundation, the Boninchi Foundation, and the EMBO Young Investigator Program (A.B. and M.S.). A.K. was supported by a Swiss Government Excellence PhD Scholarship (ESKAS-2021.0329) of the Swiss Federal Commission for Scholarships for Foreign Students. C.M., K.V.h. and S.B. acknowledge the Research Council of the Vrije Universiteit Brussel for the financial support through the Strategic Research Program (SRP50 and SRP95) and the Research Foundation Flanders (FWO) Hercules MZW OZR3939 grant. We thank members of the Stoeber and Boland groups for critical comments on the manuscript. Molecular graphics and analyses performed with UCSF ChimeraX, developed by the Resource for Biocomputing, Visualization, and Informatics at the University of California, San Francisco, with support from National Institutes of Health R01-GM129325 and the Office of Cyber Infrastructure and Computational Biology, National Institute of Allergy and Infectious Diseases.

Author contributions

J.Y. purified and reconstituted the NbE-μOR-NabFab complex and determined the cryo-EM structure. A.K. characterized NbE, receptor mutants, and peptidomimetics. X.Z. and P.R. performed GCI affinity measurements. C.M., K.V.h. and S.B. designed and synthesized peptide mimetics. A.M. and A.K. determined the NbE crystal structure. T.L. and J.S. generated NbE and performed binding characterization. All authors planned experiments and analyzed data. A.B. and M.S. supervised the project and wrote the manuscript with input from all other authors.

Competing interests

M.S., A.B., S.B., A.K., J.Y., K.V.h. and C.M. have filed a priority patent application around the new cyclic peptides targeting the μOR on Sep 12, 2024, with filing number EP24200109.7. The remaining authors declare no other competing interests.

Additional information

Supplementary information The online version contains supplementary material available at https://doi.org/10.1038/s41467-024-52947-6.

Correspondence and requests for materials should be addressed to Andreas Boland or Miriam Stoeber.

Peer review information *Nature Communications* thanks Christophe Stove, Fei Xu and the other, anonymous, reviewer(s) for their contribution to the peer review of this work. A peer review file is available.